Synthesis and Characterization of Zinc Stannate Nanomaterials for Humidity Sensing Applications

M.Tech. Thesis

By

Rituraj Verma

DISCIPLINE OF METALLURGY ENGINEERING AND MATERIAL SCIENCE

INDIAN INSTITUTE OF TECHNOLOGY INDORE

JUNE 2017

Synthesis and Characterization of Zinc Stannate Nanomaterials for Humidity Sensing Applications

A THESIS

Submitted in partial fulfilment of the requirements for the award of the degree

Master of Technology
in
Metallurgy Engineering and Material Science
by
Rituraj Verma

DISCIPLINE OF METALLURGY ENGINEERING AND MATERIAL SCIENCE

INDIAN INSTITUTE OF TECHNOLOGY INDORE

INDIAN INSTITUTE OF TECHNOLOGY INDORE

CANDIDATE'S DECLARATION

I hereby certify that the work which is being presented in the thesis entitled **Synthesis and Characterization of Zinc Stannate Nanomaterials for Humidity Sensing Applications** in the partial fulfilment of the requirements for the award of the degree of **Master of Technology** and submitted in the **Discipline of Metallurgy Engineering and Material Science, Indian Institute of Technology Indore**, is an authentic record of my own work carried out during the time period from July 2015 to July 2017. Thesis submission under the supervision of **Dr. Parasharam M. Shirage**, Associate Professor, Discipline of Metallurgy Engineering and Material Science.

The matter presented in this thesis has not been submitted by me for the award of any other degree of this or any other institute.

Signature of the student with date
Mr. Rituraj Verma

This is to certify that the above statement made by the candidate is correct to the best of my knowledge.

Signature of the Supervisor
Date:
Dr. Parasharam M. Shirage

Rituraj Verma has successfully given his M.Tech. Oral Examination held on **23 June 2017**.

Signature of Supervisor of M.Tech. thesis
Date:

Convener, DPGC
Date:

Signature of PSPC Member 1
Date:

Signature of PSPC Member 2
Date:

ACKNOWLEDGMENTS

I would like to thank all those people who made this thesis possible and an unforgettable experience for me. This work is a result of the efforts of many individuals, who helped me mentally or physically or both to successfully complete it.

First of all, I would like to express my deepest sense of gratitude to my supervisor Dr. Parasharam M. Shirage, who offered his continued advice and encouragement throughout the course of this thesis. I thank him for the systematic guidance and great effort he put in. I feel greatly privileged to be one of his students.

I acknowledge my gratitude towards Dr. Santosh Hoshmani, and Dr. Sumanta Samal my PSPC members for their kind suggestions and support during the various presentations of this work.

I am grateful to Sophisticated Instrumentation Centre (SIC), IIT Indore for providing the P-XRD, FE-SEM, TGA, BET facility equipped there. I am thankful to IIT Indore for giving me an opportunity to carry out the research work and providing all the facilities.

I would like to express my very sincere gratitude to Mr. Alfa Sharma for the experimental and technical assistance to my project to make this thesis possible. His involvement in the work from the first day I joined, to the last is highly acknowledged. I would also like to express my thanks to all members of Advance Functional Materials lab for their moral support and the friendly atmosphere they have created in the lab.

Finally, I take this opportunity to express the profound gratitude from depth of my heart to my beloved parents and my family for their love and continuous support - both spiritually and materially. The support and love they provide to chase my dream is unmatched.

ABSTRACT

Humidity sensors have drawn huge attention and became extensively important integrated device to use in our daily life for monitoring the environmental moisture for human comfort. Humidity sensors are also useful for online monitoring of the automotive, medical, construction, semiconductor, meteorological and food processing industries. The deployment of any sensor in the detection of actual humidity and environmental monitoring under various conditions demands for the quality control, high sensitivity and selectivity, fast response/recovery times, low hysteresis, high stability, serviceability in wider humidity range and temperature, miniaturization and economic viability, *etc.* The opportunities to achieve these features by sensors based on bulk materials under real time monitoring conditions are hindered by the unpredictable humidity levels present in the environment. However, chemically and thermally stable metal oxide nanostructures, known to provide larger surface-to-volume ratio for interaction with the environment are observed to be suitable candidates for humidity sensing with high sensitivity, fast response than that of bulk materials. In recent years, metal oxide nanostructures such as ZnO, SnO_2, TiO_2, In_2O_3, and WO_3 are utilized for the fabrication of variety of chemical sensors. But the presence of single cation site and high temperature operation restricts its much needful requirement.

Zinc stannate, a multifunctional ternary metal oxide material, exists as two types of oxide with different Zn/Sn/O ratios ($ZnSnO_3$ and $Zn2SnO_4$), which have potential applications in lead-free ferroelectrics, transparent conductors, photo catalysts, dye-sensitized solar cells, gas sensors, and lithium ion batteries (LIBs). Recently, $ZnSnO_3$ nanostructures using various synthesis routes have drawn attention for obtaining better crystallites. However, the synthesis of composite metal oxides is particularly challenging in water due to variation in precursors reactivity. To overcome this here we report the synthesis of Zinc Stannate nanoparticles utilizing wet chemical synthesis method with variation in synthesis temperature which helps to get crystallites after annealing at different temperature.

For evaluation of structural and morphological properties of prepared $ZnSnO_3$ samples, X-ray diffraction (XRD) and scanning electron microscopy (FE-SEM) are implemented. To analyse the thermal behaviour TGA-DSC and for surface porosity Brunauer–Emmett–Teller (BET) and the Barrett–Joyner–Halenda (BJH) methods,

respectively are used. The humidity sensing of all the samples were performed on indigenous developed humidity sensor testing setup within a wide range.

Annealing effect has prominent role over the physical and sensing properties of the as prepared samples. XRD and FE-SEM confirms the sequential growth of $ZnSnO_3$ crystallites into much uniform crystalline cubes of nearly 100nm with implementation of annealing temperature from 250°- 500°C. TGA and differential TGA study over the as prepared samples shows overall 19% weight loss due to removal of water molecules within 0-600°C temperature range after which no such loss is visible suggests the optimal thermal treatment temperature. Similarly, on carrying out the N_2 adsorption-desorption study over the $ZnSnO_3$ samples shows surface area of 17.18 ,19.99 and 15.55 m^2/g for samples prepared at a stirring temperature of 65°C, 85°C and 100°C respectively. On implementation of the as prepared and different annealed samples towards humidity sensing in a range of 08-97% RH value, better sensitivity factor of around 700-4500% is observed in case of 500°C annealed $ZnSnO_3$ samples. The hysteresis error calculation for the 500°C annealed samples showed much lower value i.e. about 0.000003 at 97% RH and practically none of the sample shows significant hysteresis value over the applied humidity range promoting it device usage.

To investigate the isotherm behaviour of $ZnSnO_3$ samples and to confirm the water adsorption-desorption mechanism which takes place in humidity sensing, Freundlich isotherm modelling of all the samples using relative deviation in resistance (R.D.R) against applied relative humidity was done. The results inferred that 500°C annealed samples show 87-97% deviation in resistance value from the initial value at ambient along with higher adsorption strength and adsorption capacity value of 2.5 and 9.5 respectively. The linear fitting of experimental results clearly shows presence of two adsorption regions in all the samples supporting the plausible humidity sensing mechanism and ZnSnO3 turns out to be excellent humidity sensing material.

TABLE OF CONTENTS

LIST OF FIGURES

LIST OF TABLES

Chapter 1

1. Introduction

1.1. Humidity and its measurement

Humidity, which is amount of water vapor present in air or atmosphere, is highly variable and changes according to seasons, land, sea, temperature and so on, and has an important role in the quality of industrial products, advanced instruments and human life. The regulation of humidity is important for human comfort, storage of various goods, industrial process control, high-tech instruments, and plenty of advanced sectors. Humidity sensors with high sensitivity, stability and economical are in high demand in industries of automated devices, food processing, automotive manufacturing, pharmaceutical processing and also weather forecasting. There are two main types of humidity sensing materials, which are ceramic and polymer-based materials. Generally, the metal oxide ceramic type humidity sensor is highly stable and has faster response compared to the polymer-based humidity sensor.

In industry, optimum humidity conditions should be provided on production lines for obtaining high quality products. For example, in textile processing, generation of electrostatic charges during the fabrication may cause the materials to cling. This is prevented by keeping the environment in damp conditions. On the other hand, dry conditions are required during processing of silicon wafers in a clean room, assembling electrical products on the assembly line and so on. In the automobile industry, humidity sensors are used in rear window defoggers and motor assembly lines. In the agriculture sector, since adequate environmental humidity conditions are needed to grow fruits and vegetables, similar conditions are needed in the preservation of different types of foods and cottons.

There are many domestic applications, such as cooking control for microwave ovens, intelligent control of laundry and the living environment in buildings, and intelligent control and so on. In the medical field, humidity sensors are used in respiratory equipment, sterilizers, and incubators, pharmaceutical processing, and biological products. Thus, the measurement and control of humidity have significant importance in many areas for different purposes.

In 1450, Nicolas Cryfts invented a hygrometer which is the first humidity measurement instrument on record. This hygrometer used wool to determine the changes of humidity in air. Over the past 550 years, many other kinds of hygrometer have been invented.

Vapor pressure (hPa) is a partial pressure of water vapor in the air. Saturation vapor pressure is measured on a surface of water or ice at thermodynamic equilibrium condition. Dew point is a temperature, above 0 °C, at which the air will be cooled down to reach saturation at constant pressure condition and it is generally equal to or lower than the actual air temperature. Frost point is a temperature, below 0 °C, at which moist air saturates with respect to ice. [1]

Humidity can also be expressed in other ways like absolute humidity (g/m^3), defined as the amount of water vapor contained in a unit volume of dry air, i.e., mixing ratio (parts per million by volume, ppmv) and the ratio with respect to saturation is defined as saturation deficit p_{sd} (mbar). To know the effect of different doping elements or materials in the sensor materials is most vital part of humidity sensor development for the different applications.

1.2. Miniaturized Humidity Sensors

For many sophisticated applications, there has been a keen attempt to reduce the size of the sensors using the most advanced technologies collectively called miniaturization. Miniaturized humidity sensors mainly depend on five different transduction principles: hygrometry, capacity, resistance, gravimetry and optical properties.

1.2.1. Hygrometric Sensors

For many decades, hygrometric sensors have been using in old devices that are classified into four basic types—mechanical, dry bulb-wet bulb, chilled mirror, LiCl dew point—for the measurement of the humidity of air, which is converted into mechanical energy.

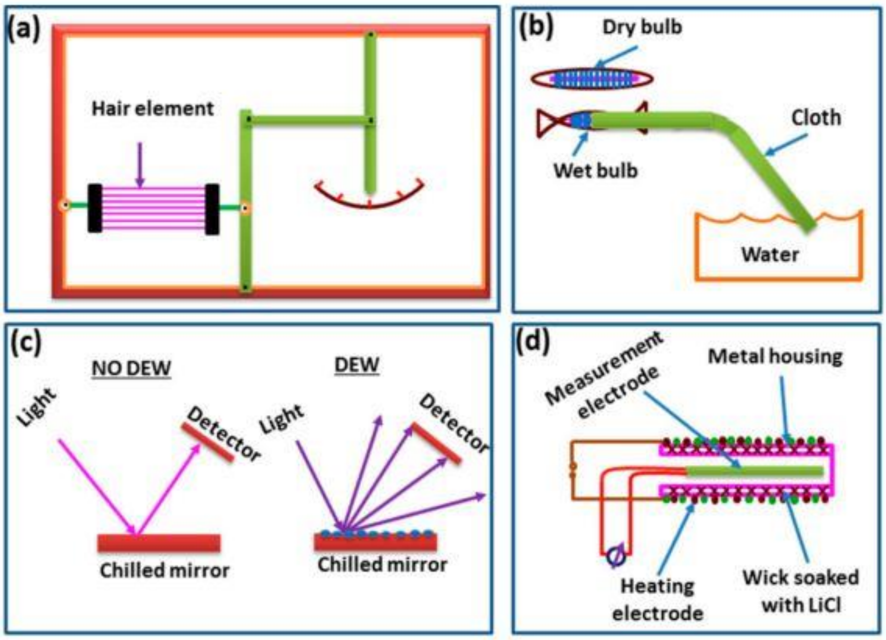

Figure 1.1 Working of Hygrometric Sensors

Generally, hygrometric sensors have two different materials with different thermal expansions coefficients, such as a polysilicon membrane and a hygroscopic material such as polyimide.

Advantages:

- Low cost;
- It provides a primary rather than a secondary measurement of dew point;
- High accuracy;
- High repeatability;
- Wide temperature range;
- Low hysteresis;

Disadvantages:

- More complex, may be more expensive;
- Narrow flow rate range;
- Periodic cleaning may be required;
- High uncertainty (±2% to 5%).

1.2.2. Resistive Sensors

The most common resistive sensors are based on electrical resistance. The electrical resistance of a material is the opposition to the passage of an electric current through that conducting material. Generally, the all resistive sensors have four layers: substrate, interdigital electrode, humidity sensitive film and protective layers. In resistive or impedance humidity sensors, air humidity changes with the variation of resistance and follows Equation (1.1).

$$Log(\frac{R(r_h)}{R_0}) = \frac{loga - logr_h^n}{1 + b/r_h^n} \qquad (1.1)$$

where R (r_h) represents the resistance at relative humidity (RH) at a specific humid condition r_h , R_0 is the resistance at zero humidity, and *a* and *b* are the constants.
The sensing response (S_R) can be measured using an expression given in Equation:

$$s_R = \frac{R_h - R_0}{R_0} x100 \qquad (1.2)$$

where R_h refers to the resistance at certain humidity and R_0 represents the original resistance of the sensors at air of 3% RH.

Advantages:

- Small and cheap;
- Mass production possible;
- Interchangeable/field replaceable.

Disadvantages:

- Limited range (typically 15% to 95% RH);
- High temperature dependency;
- Sensitive to contamination, condensation;
- Resistive type sensors find difficulty in measuring low values (below 5% RH);
- The change in impedance is too high and hence it is difficult to control the dynamics and temperature effects significantly.

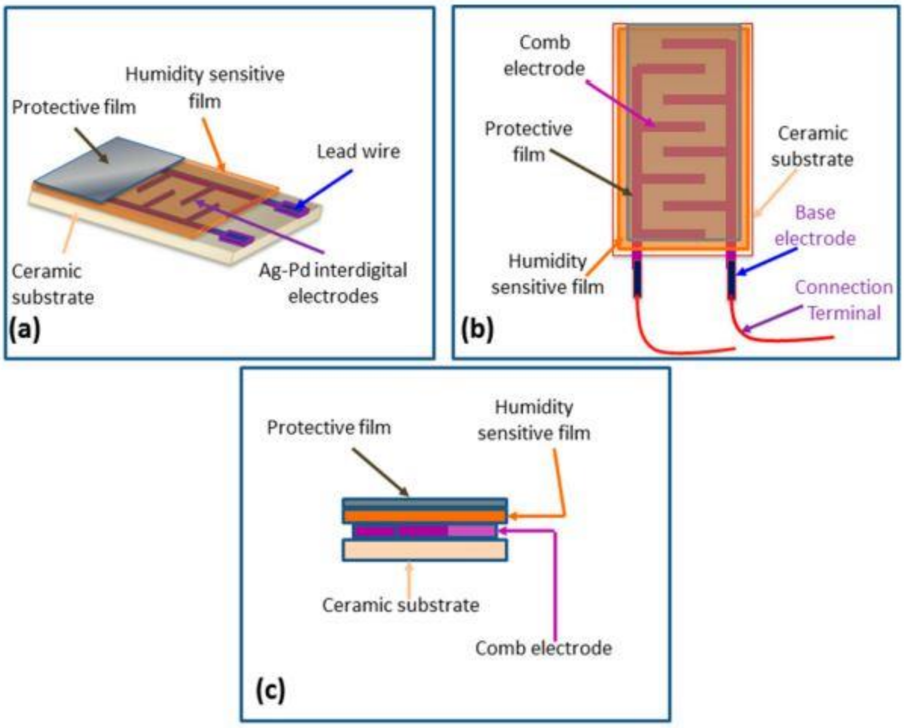

Figure 1.2 Different views of resistive type humidity sensors: (a) isometric view; (b) top view; (c) cross-sectional view.

1.2.3. Capacitive Sensors

The capacitance of a sensor indicates the ability of a body to store an electrical charge. It can change significantly with humidity. Using this principle, capacitive type humidity sensors have been developed. Their characteristics mainly depend on the hygroscopic nature of the material and the geometry of the electrode. In this regards, capacitance (C) of all the parallel plate capacitive sensors follows a relation given by Equation 1.3:

$$C = \frac{\epsilon A}{d} \tag{1.3}$$

where ϵ is the dielectric permittivity, A is the overlapping area, and d is the distance between two parallel plates. The sensitivity (Sc) of this capacitive humidity sensor is evaluated using Equation (1.4) within a certain range of humidity:

$$Sc = \frac{Maximum\ Capacitance}{Minimum\ Capacitance} \tag{1.4}$$

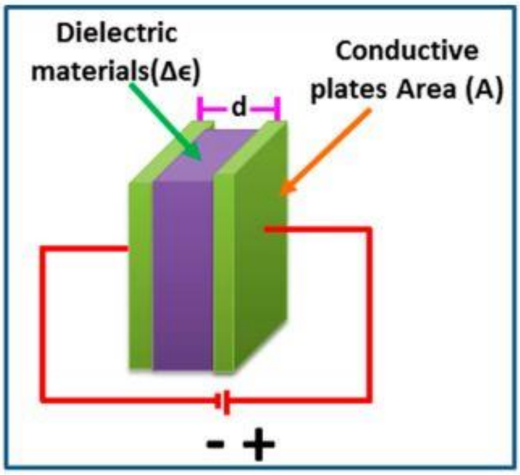

Figure 1.3 Basic schematic diagram of a parallel plate capacitor.

A capacitive type humidity sensor based on gold-poly (vinyl alcohol) (PVA) encapsulated gold (Au) nanoparticle nanocomposites (NCs) was analysed by Yao *et al.* [2]. Here, Au-PVA core-shell NCs were used as dielectric material in between the electrodes. In most capacitive sensors, different types of polymers or elastomer-based materials are used as dielectric materials. An ultra-thin flexible capacitive humidity sensor was designed by Pantalei *et al.* [3].

Advantages:

- Wide measurement range 0%–100% RH;
- Wide temperature range (up to 200 °C);
- Full recovery from condensation;
- Highly resistant to contaminants;
- Small in size;
- Low cost;
- Require very little maintenance.

Disadvantages:

- Can be limited by distance from electronics to sensor;
- Loss of relative accuracy at low end (<5%);
- Requires electronics to convert capacitance to relative humidity;
- Significant drift.

1.2.4. Gravimetric Sensors

The quartz crystal microbalance (QCM) is the main source of inspiration for gravimetric sensors. This sensor consists of a piezoelectric quartz plate, which is coated with a hygroscopic material having resonance frequency in the MHz range, and it measures humidity due to the change of frequency as shown in Figure 1.4. The change of frequency (Δf) can be calculated by the Sauerbrey Equation:

$$\Delta f = -2 \frac{1}{A} \frac{f_0^2}{\sqrt{\mu \rho}} \Delta m \tag{1.6}$$

where A represents the area of surface, μ is the shear modulus, f_0 is the nominal frequency, ρ is the density, Δm is the mass change due to absorption of moisture. A general schematic of a gravimetric sensor based on frequency shift detection is illustrated in Figure 1.4.

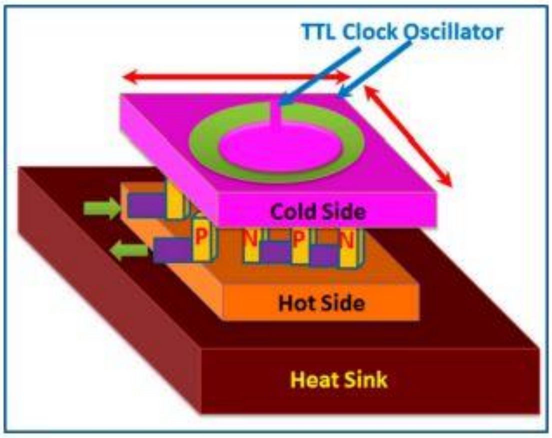

Figure 1.4 The schematic diagram of a QCM humidity sensor.

In this case, a resonance frequency shift occurs due to the absorption of mass in the chemical layer which is recorded by the resonator. The gravimetric sensor has some advantages as well as some disadvantages which are listed below:

Advantages:

- Relatively low response time;
- Good accuracy;
- Low drift.

Disadvantages:

- Nonlinear characteristics;
- High temperature dependence;
- Require complicated systems for signal processing of sensor outputs.

1.2.5. Optical Sensors

All the above discussed humidity sensors have their own transduction principles to measure the humidity with some advantages and disadvantages. Normally electronic devices related to the above sensors cannot work under electromagnetic interference or in remote monitoring systems and hazardous or explosive environments. However, optical sensor-based humidity sensors are ideal devices to work under the above severe conditions, thus they see significant use in many advanced applications where they show enhanced efficiency. The reflected optical power (I) due to the perpendicular light impingement from the interface depends on the refractive indices n_1 and n_2 of the two media and follows Equation (1.7):

$$I = I_0 \left[\frac{n_2 - n_1}{n_z + n_1}\right]^2 \tag{1.7}$$

where I_0 is the optical power monitored from the reference signal.

A porous sensing film of silica xerogel on the tip of an optical fiber provides an optical cavity where the fiber-xerogel interface gives the first refection and the xerogel-vapour interface gives the second reflection.

Figure 1.5 Image of a fiber optic humidity sensor

The changes in the reflectance at the fiber-film and film-external medium interfaces also vary with film thickness

Advantages:

- Low cost;
- High sensitivity;
- Robustness;
- Flexibility;
- Ability for remote monitoring as well as multiplexing;

Disadvantages:

- Inherent losses;
- Dispersion;
- Nonlinearity;
- Birefringence.

1.2.6. Mechanical-Optoelectronic Humidity Sensors:

In addition to the abovementioned five main types of humidity sensors, they can also be categorized by principle, which is the mechanical-optoelectronic principle, as shown in Figure 1.7. This device consists of a light emitting diode (LED), a very sensitive photodiode, and a mechanical system. When the humidity concentration changes the contraction and expansion occurs in the hair, this hair pulls the metal sheet up or down. Thus, the window opening area changes and this varies the light intensity reaching the photo detector from the LED, resulting in a photocurrent change with respect to humidity on the output side.

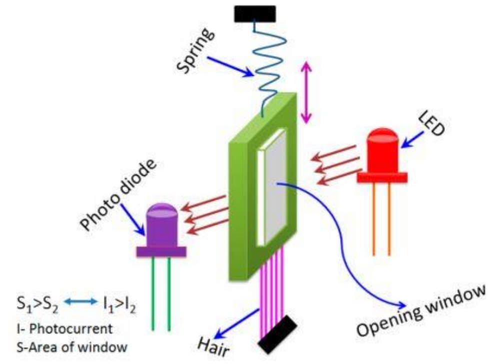

Figure 1.6 Schematic representation of a humidity sensor that operates by the mechanical-optoelectronic principle.

Chapter 2

2. Literature Review

2.1. Humidity sensing Mechanism

Humidity sensors based on water-phase protonic materials are used widely in industry and research laboratories. The adsorbed water condensed on the surface of the materials and protons will be conducted in the formed aquatic layers. For ionic sensing materials, if the humidity increases, the conductivity decreases and the dielectric constant increases. In bulk water, proton is the dominant carrier responsible for the electrical conductivity. The conduction is due to the Grotthuss mechanism, through which protons tunnel from one water molecule to the next via hydrogen bonding that universally exists in liquid-phase water.

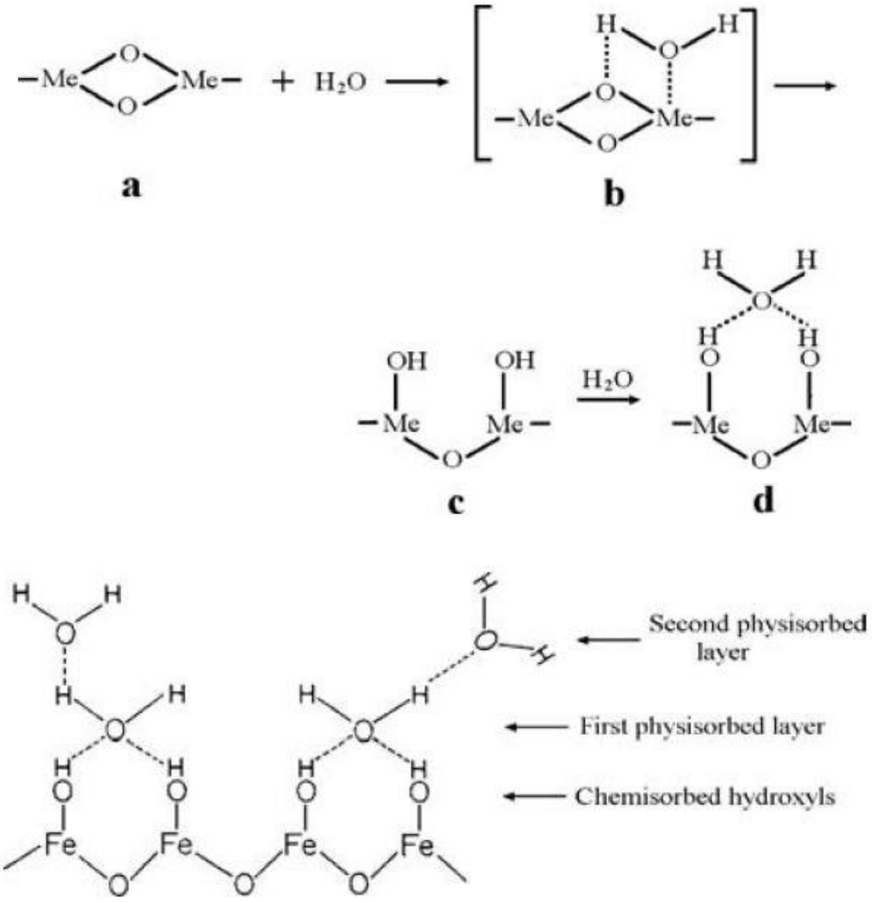

Figure 2.1 Brief illustration of the Grotthuss mechanism

As water continues to condense on the surface, an extra layer on top of the first physically-adsorbed layer forms. This layer is less ordered than the first physically-adsorbed. The second physisorbed layer, water molecules become mobile and finally almost identical to the bulk liquid water, and the Grotthuss mechanism becomes dominant. This mechanism indicates that sensors based purely on water-phase protonic conduction would not be quite sensitive to low humidity, at which the water vapor could rarely form continuous mobile layers on the sensor surface. The two immobile layers, the chemisorbed and the first physisorbed ones, while cannot contribute to proton-conducting activity, could provide electron tunnelling between donor water sites. The tunnelling effect, along with the energy induced by the surface anions, facilitates electrons to hop along the surface that is covered by the immobile layers and therefore contributes to the conductivity. This mechanism is quite helpful for detecting low humidity levels, at which there is not effective protonic conduction.

2.2. Important oxide-based materials and their humidity sensing properties

During the last five decades, plenty of sensing materials have been developed for different types of humidity sensors in a wide range of applications. The most common commercial sensors are mostly based on metal oxides, porous silicon and polymers. In a humidity sensor, fundamentally, the humidity signals obtained via two-electrode techniques are affected by polarization effects.

Although humidity sensors based on different materials have been used for more than six decades, the key factors to improve sensing characteristics in different applications are still not well defined. This is extremely important in the miniaturization of sensors in nanotechnology for many advanced applications. Therefore, based on different materials, the plots of the important electrical characteristics of various morphological structures, coatings or doping agents are recognized and typically compared.

2.2.1. Al_2O_3

Al_2O_3 is one of the most favourable ceramic sensing materials due to its independence of temperature at nearly all range of relative humidity from 25˚C to 80˚C. The crystal content is quite small and amorphous Al_2O_3 formed by anodization or vacuum deposition contains γ-phase to some degree, whereas the former is crystalline and the latter has no significant peaks in X-ray diffraction except for one broad peak. Many of the present Al_2O_3 humidity sensors are fabricated through anodization. Because of its low-cost and easy process, anodic Al_2O_3 has great priority over other ceramics. [3]

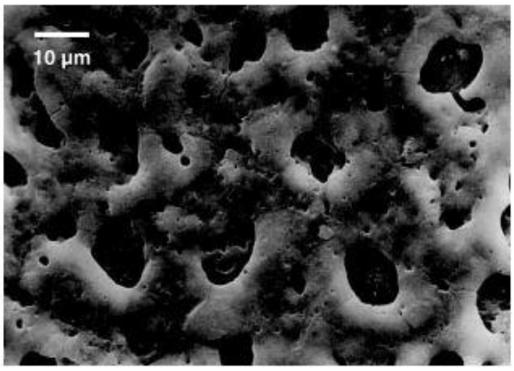

Figure 2.2 Porous Al_2O_3 by anodic spark deposition.

The primary problem of anodized amorphous Al_2O_3 as discussed that when exposed for a long duration in high humidity, significant degradation in the sensitivity and drift in the capacitance characteristics would be expected. This was attributed to the widening of the pores due to diffusion of the adsorbed water.

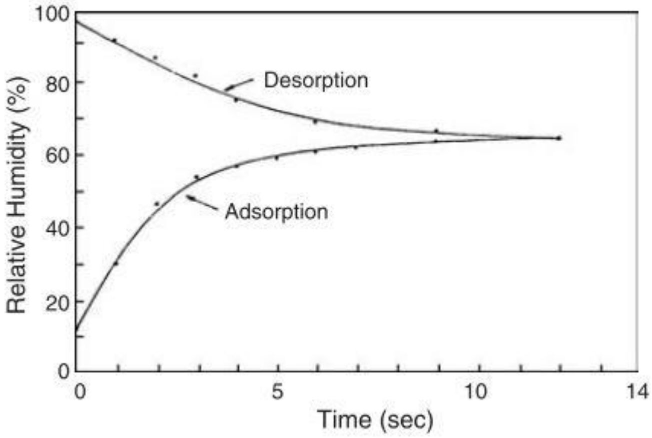

Figure 2.3 Time responses of the α-Al_2O_3 sensor to relative humidity from 12% to 65% and from 95% to 65%.

The best solution would be to grow self-ordered porous films and eliminating the variability among the pores and irregularities the microstructure of the film. Thermal annealing at about 400˚C has been reported to have limited improvement of the stability of anodized Al_2O_3 sensors

2.2.2. TiO_2

TiO_2 has three phases: anatase, rutile, and brookite. The third one is seldom used in humidity sensing. When heated strongly (~ 1000˚C), anatase automatically transforms to the rutile structure. Rutile is the most common phase of TiO_2, while anatase is very rare in nature. At high temperature (~ 600˚C), anatase is an *n*-type semiconductor but rutile is a *p*-type one. Their sensing responses to reducing gases like H_2 usually behave on the opposite directions. However, because humidity sensing is usually realized by the adsorbed proton-conducting water layers on the porous structure at room temperature, both phases should behave approximately the same in resistance or capacitance changes.

However, most TiO_2-based sensors using the above fabrication methods are not sensitive at low humidity levels and have limited detection ranges from 10% to 30%RH. A newly developed TiO_2 nanowire sensor is only capable to detect relative humidity levels down to11%. For K+-doped TiO_2 film sintered at a temperature below 500˚C, it is capable to sense humidity levels lower than 10%. In addition to resistive/capacitive sensors, sensors based on magneto-elastic method was found to be sensitive to a humidity level of 2% RH, in which the change of mass of TiO_2 (pore size around 80 nm) due to water-adsorption is measured. [29]

2.2.3. SiO_2

Although SiO_2 grown by wet or dry oxidation has been used as an insulator in electronics for a long time, it is definitely not suitable for humidity sensing because it is a dense material. Humidity sensors based on porous silicon oxide were fabricated using bulk-sintering processes, especially traditional sol–gel method, in which SiO_2 is precipitated by hydrolysis of certain alkoxide of silane. Nonetheless, the most prominent merit of SiO_2 as a humidity sensing material is its compatibility with the current microelectronics industry. Similar to other porous ceramic materials, the humidity sensitivity of SiO_2 can be enhanced by adding electrolyte dopants, e.g., LiCl. Although it was reported that sol–gel fabricated SiO_2 sensor could detect humidity as low as 4% RH, most reported works showed that only humidity over 20% RH can be detected. During the last few years, humidity sensors based on silicon monoxide (SiO), a powder that is used as a coating material, have been prepared by a novel film fabrication method, glancing angle deposition (GLAD). In this method, the substrate is highly oblique to the incident vapor flux and isolated columns of the material deposited grow toward the vapor source. It is possible to control the film microstructure on a 10 nm scale [11]. Although the SiO films deposited by GLAD are not sensitive to humidity levels lower than 15% RH, the response and recovery times are as short as in milliseconds. These may be the fastest humidity sensors ever reported.

2.2.4. Spinel Compounds

The spinel compounds belong to a large group of oxides with a general composite of AB_2O_4. A can be a divalent metal element, especially in group II, group IIB, and VIIIB. X generally represents a trivalent metal, e.g., iron, chromium, and aluminium. The structure of this group is tetrahedron always with high density of defects.

Although spinel oxides are semiconductors, most of the reported humidity sensors based on these materials have ionic sensing properties probably due to their low operating temperatures (<100˚C). In case that the pore size is very small (100 ~ 300 nm), the lower detection limit can be down to 1% RH. Like other humidity sensing ceramics based on proton-conducting mechanism, doping with alkali ions facilitates formation of hydrated protons. Similar to perovskite oxides, spinel oxides are fabricated by bulk-sintering of the mixture of two metal oxides [13].

2.2.5. SnO_2

Stannic oxide (SnO_2) is an *n*-type wide-bandgap semiconductor. H_2O is adsorbed on the oxide surface in molecular and hydroxyl forms and the mechanism was identified to be electronic. A more complicated SnO_2 –H_2O inter-action model was constructed on considering of water desorption in molecular form, dissociative chemisorption and desorption of OH−groups. The water molecule still behaves like a donor on the SnO_2 surface. Different from TiO_2 and other high-temperature semiconducting ceramics, SnO_2 shows electronic conductivity at rather low temperature (even at room temperatures) [14].

For sensors based on In_2O_3 or ZnO, similar peak patterns due to step-like humidity changes were also observed in the temperature range from 230˚C to 540˚C. The mechanism should be similar to that of SnO_2 sensors. For sensors based on ultra-thin SnO_2 films (60–90 nm) prepared by sol–gel process, the response time ranged from 8–17s for different humidity changes and the recovery time was only about 1 s, due to their ultra-thin films. However, most reported SnO_2 sensors are only sensitive to RH higher than 30%. In addition to sensing water vapor, SnO_2 is widely used for multiple gases, especially harmful oxides such as NO_X, CO, PbO_2. Since these sensors are usually operated at temperatures above 200˚C, heaters are always attached at the backside.

2.2.6. Perovskite Compounds

The perovskite compounds belong to a large group of oxides with a general composition of AXO_3. The A can be any metal element with + 2 valence electrons, e.g., group II, group IV, and rare earth metals. The X represents titanium, niobium, and iron. Sometimes A or X could be a combination of two or more elements, e.g., $La_{0.7}$ $Ca_{0.3}$ for A and $Zr_{0.2}Ti_{0.8}$ for X. [15] All members of this group have the same basic structure that is isometric. At room temperature, some porous perovskite oxides still demonstrate humidity sensitivity, e.g., $BaMO_3$ (with M = Ti, Zr, Hf, or Sn).

Because the sensing mechanism is no longer electron-conducting but ion-conducting, they are only sensitive to humidity higher than 8%–20% RH. In these cases, the porous perovskite oxides operating at room temperature may be regarded as simple resistive/capacitive ceramics, in which the group II elements may serve as metal ions to improve the conductivity in moisture. Most humidity sensitive perovskite oxides were fabricated by bulk-sintering of the mixture of two or more metal oxides/carbonates.

2.2.7. In_2O_3

In industry, smooth and transparent films made of indium oxide, an *n*-type ceramic semiconductor, are used as infrared-reflectors or electrodes for liquid crystals. There are a couple of methods for fabrication of rough and porous In_2O_3 layers that are sensitive to moisture. Laser ablation was reported to be a good method to sensitize ITO to humidity by producing gaps on the substrate layer.

Figure 2.4 $Ba_{1-x}Sr_xTiO_3$ sintered at 1050 ˚C [4]

The humidity-sensing is due to the porous water- adsorbing structure inside the gaps. The *p*-type doping with divalent anions from the VIII group (Mn^{2+}, Ni^{2+}, *etc.*) may also facilitate the roughness and porosity. Using thermal deposition in high vacuum was found to obtain In_2O_3 films with granular sizes ranging from 1 to 10 µm. However, none of the presented In_2O_3 humidity sensors are able to sense relative humidity lower than 25% and the response may take a couple of minutes [16]. This type of devices still needs improvement. Although we categorize In_2O_3 as a semiconducting (electronic conducting) material, its moisture-sensing mechanism is still not very clear.

2.2.8. Review on $ZnSnO_3$ as Humidity Sensor

S. Aziz *et al.*, [30] discussed about transfer printing based device containing PEDOT: PSS and $ZnSnO_3$ nanocomposite for humidity sensing purposes. They observed that the device shows an impedance change from ~18 MΩ to 1.8 MΩ by moving from 0% to 90 % relative humidity zone for a longer period with negligible change.

J. Li *et al.*, [31] reported highly sensitive Sb- doped $ZnSnO_3$ nanoparticles prepared by dual hydrolysis assisted liquid precipitation reaction and hydrothermal procedure. The obtained Sb-doped $ZnSnO_3$ NP's showed 130% higher humidity sensitivity at 30% RH than that at 85%. Even the response and recovery time reported for the sensor is 7.5s./33.6s. on switching it between 30% to 85% relative humidity range.

N. D. Md Sin *et al.*, [32] described the synthesis procedure for $ZnSnO_3$ thin films by using sol-gel immersion method by varying deposition time. They concluded that the sample with 2hrs. deposition time showed better sensitivity along with faster response change in air, good repeatability and stability which can be inferred to the well-developed nanocubes like morphology.

B.C. Yadav *et al.* [33] Synthesized different compositions of zinc stannate by using chemical co-precipitation method. The samples undergone through thermal treatment at 600°C, XRD provides information regarding the average particle size of 4 nm with well-developed nanocrystalline $ZnSnO_3$ of perovskite phase with orthorhombic crystal structure. The zinc stannate composition of 1:4 were found to be more sensitive towards humidity with sensitivity factor of 3GΩ/% RH along with stability retention of 72%

D. Bauskar *et al.,* [34] reported hydrothermal synthesis of $ZnSnO_3$ cubic crystallites. The zinc stannate cubes in form thin film shows an excellent humidity sensing features like response and recovery time of 7 s./16 s., hysteresis limit of 3.5%

CHAPTER – 3

3. Synthesis and Characterization

3.1. Synthesis of $ZnSnO_3$ Crystallites

The $ZnSnO_3$ crystallites synthesized using simple wet chemical method where only stirring temperature was varied during the process. The obtained $ZnSnO_3$ nanomaterials are indicated as S-01, S-02, S-03 S-04 and S-05 where the stirring temperature maintained at 25°C, 45°C, 65°C, 85°C and 100°C respectively. The above stated notation is carried out further in the report with its basic meaning. All the reagents were of analytical grade from Sigma-Aldrich Co.Ltd., which are used without any further purification. In a typical experiment for the synthesis of $ZnSnO_3$ crystallites, 10mmol of Zinc sulphate heptahydrate ($ZnSO_4.7H_2O$) were dissolved in 100 mL of double distilled water, and the solution was stirred at room temperature until clear solution obtained. Similarly, 10mmol of sodium stannate ($Na_2SnO_3.3H_2O$) was added in 20mL double distilled water and stirred upto a clear solution. Then the sodium stannate solution was added to the zinc sulphate solution and the mixed solution is stirred vigorously at 25°C for 6 hours. The molar ratio of zinc sulphate heptahydrate and sodium stannate is maintained 1:1.

After the reaction, the precipitates were collected by centrifugation at 10,000 rpm and then washed repeatedly with distilled water and ethanol for removal of any impurities from product. The final product is dried in hot oven for overnight and grinded before any characterization. The same procedure is followed during the preparation of other $ZnSnO_3$ samples where only the stirring temperature varied to 45°C, 65°C, 85°C and 100°C each time.

3.2. Materials Characterization

The crystal structure and surface morphology of $ZnSnO_3$ samples were investigated using X-ray diffraction (XRD, Bruker D8 Advanced X-ray diffractometer) with Cu-Kα radiation (λ = 1.54 Å) and field emission scanning electron microscope (FESEM, Supra 55 Zeiss), respectively. Thermogravimetric and differential thermogravimetric analysis of the prepared samples were carried out using TGA-DSC (Mettler Toledo Thermal Analyzer) at a heating rate of 5°C/min in air. The nitrogen adsorption and desorption isotherms were obtained by Quantumchrome Q_2, and the specific surface area and the pore size distribution were calculated by the Brunauer–Emmett–Teller (BET) and the Barrett–Joyner–Halenda (BJH) methods, respectively. Electrical characterizations were measured by the two-probe device which was connected to Keithley Source meter 2401 through copper clips acting as electrodes and interfacing to PC is done by LABVIEW®.

3.2.1. XRD

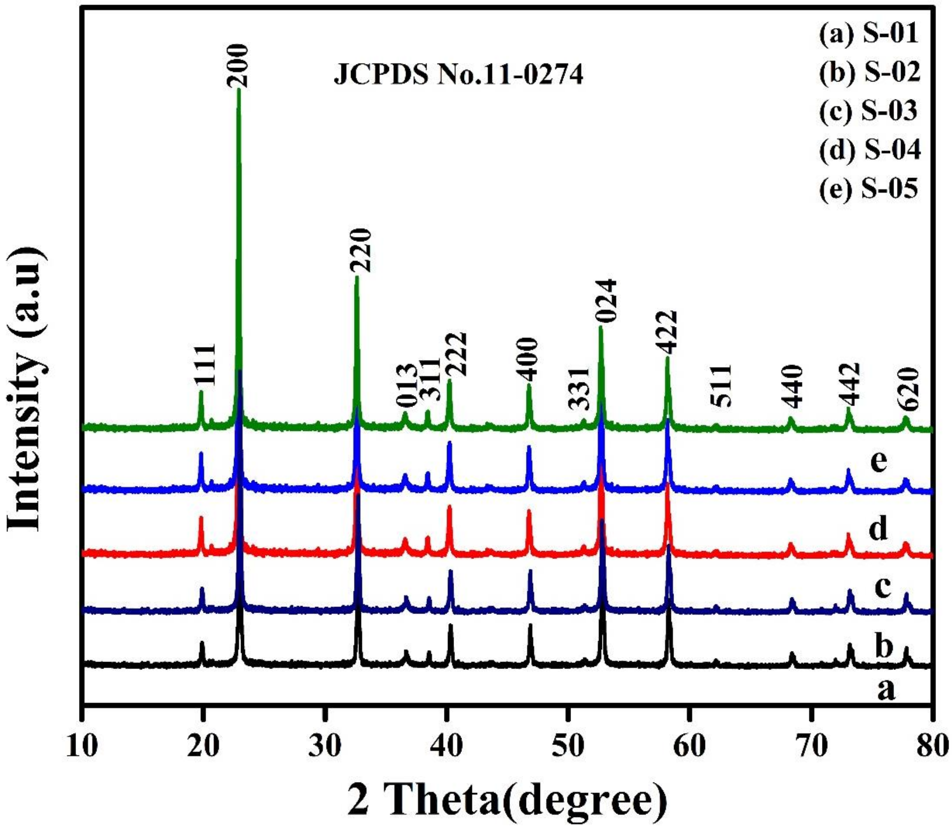

Figure 3.1 XRD patterns of $ZnSnO_3$ samples (a) S-01, (b)S-02, (c) S-03, (d) S-04 and (e) S-05 prepared at stirring temperature of 30°C, 45°C,65°C, 85°C and 100°C respectively.

The composition and phase purity of as obtained products were first examined by X-ray powder diffraction (XRD) patterns. Figure.3.1 shows that the XRD pattern of a typical $ZnSnO_3$ crystallites sample fabricated at different temperature. All of the diffraction peaks can be indexed to the standard $ZnSnO_3$ with the perovskite structure (JCPDS No.11-0274) [18]. No impurity phases were detected from the XRD pattern, indicating that $ZnSnO_3$ crystallites with high purity could be obtained under current synthetic conditions at the reaction temperature from 25 to 100°C. The samples noted as S-01, S-02, S-03, S-04 and S-05 in Fig.3.1 expresses the samples prepared at different stirring temperature maintained during the synthesis process which are 25°C, 45°C, 65°C, 85°C and 100°C respectively.

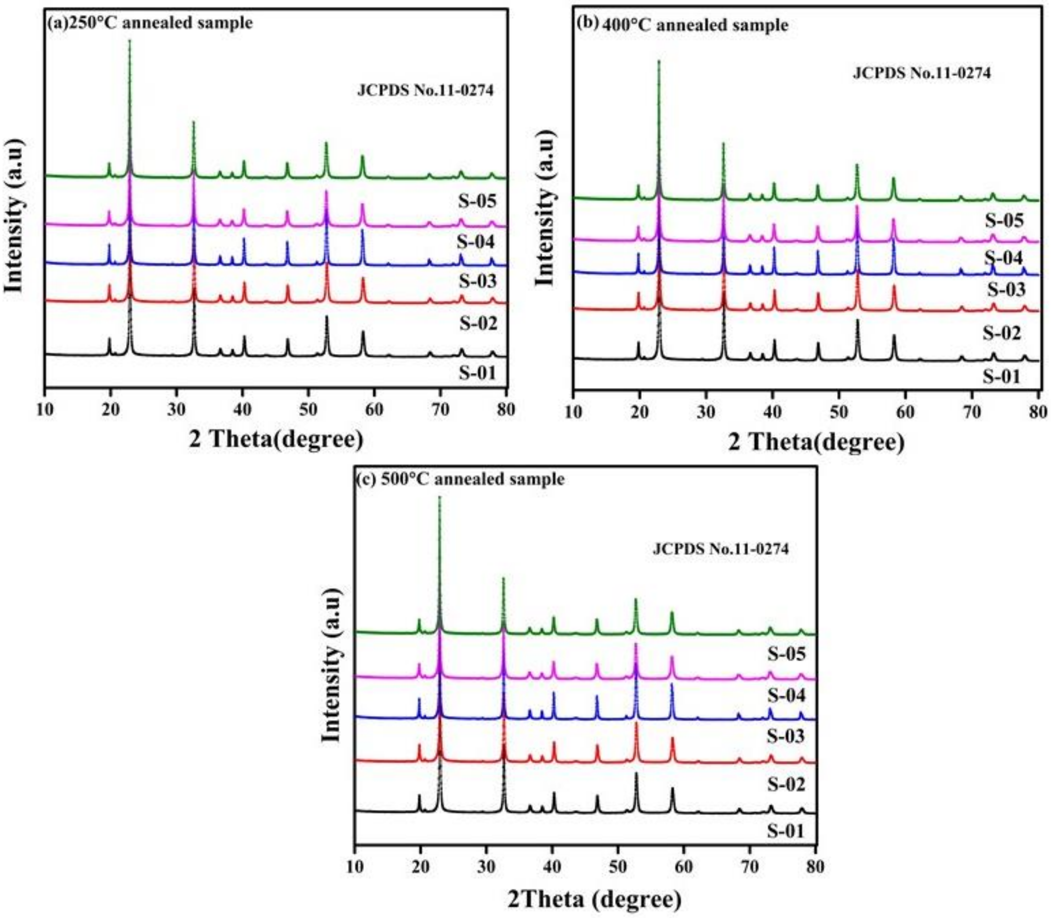

Figure 3.2 XRD patterns of (*a*) 250°C, (*b*) 400°C and (*c*) 500°C annealed $ZnSnO_3$ samples.

To further investigate the effect of annealing over the prepared samples in both aspect of structural and sensing we examined the XRD pattern of $ZnSnO_3$ annealed at 250°C, 400°C and 500°C. Here also the all of the diffraction peaks can be indexed to the standard $ZnSnO_3$ with the perovskite structure; Space group=R3c, (JCPDS No.11-0274) along with no impurity phases, indicating that $ZnSnO_3$ crystallites with high purity were obtained after the annealing. Fig.2 (*a*) shows peaks at $2\Theta = 19.82°$, 22.97°, 32.73°, 36.67°, 38.47°, 40.37°, 46.78°, 52.74°,58.34°,68.33°, 73.16° and 77.89° for peaks (111), (200), (220), (013), (311), (222), (400), (024), (422), (440), (442) and (620), respectively. Similarly, in case of 400°C annealed samples of $ZnSnO_3$ (Fig.2 (c)) peaks (111), (200), (220), (013), (311), (222), (400), (024), (422), (440), (442) and

(620) observed at 2Θ values of 19.70°, 22.85°, 32.51°, 36.56°, 38.47°, 40.15°, 46.68°, 52.84°, 58.24°, 68.33°, 73.06° and 77.77° respectively. Both in case of 250°C and 400°C annealed samples the peaks at (331) and (511) were not observed than that of as prepared samples. Whereas in case of Fig.2 (*d*) for 500°C annealed samples the peaks (111), (200), (220), (013), (311), (222), (400), (331), (024), (422), (511), (440), (442) and (620) appeared at 2Θ values of 19.84°, 22.85°, 32.75°, 36.67°, 38.47°, 40.15°,46.66°,51.27°,52.62°,58.12°,62.16°,68.33°,73.06° and 77.77° respectively. For annealed samples a slight shifting of 2Θ values is observed than that of as prepared samples.

Moreover, good crystallinity and strong structure of $ZnSnO_3$ are evidently occurred by the increase of annealing temperature as shown in XRD patterns (Fig. 1 & 2). For the confirmation of this assumption, $ZnSnO_3$ crystallite size can be interpreted from XRD peak width at 200 plane of spinel phase calculated by Scherrer equation [19];

$$D = \frac{k\lambda}{\beta cos\Theta} \tag{3.1}$$

where D is average crystallite size, κ is the shape factor (0.9), λ is the wavelength of incident x-ray Cu $K\alpha$ (λ = 1.541 Å), β is the full width at the half maximum (FWHM) on 2θ scale and θ is the Bragg's diffraction angle. The average of $ZnSnO_3$ crystallite size is approximately 66nm, 88nm, 86nm,74 nm respectively for as prepared, 250°C annealed, 400°C annealed and 500°C annealed samples. From the calculation, it can be suggested that strong crystallinity and large crystallite size of $ZnSnO_3$ is significantly changed as annealing temperature increases.

3.2.2. FE-SEM

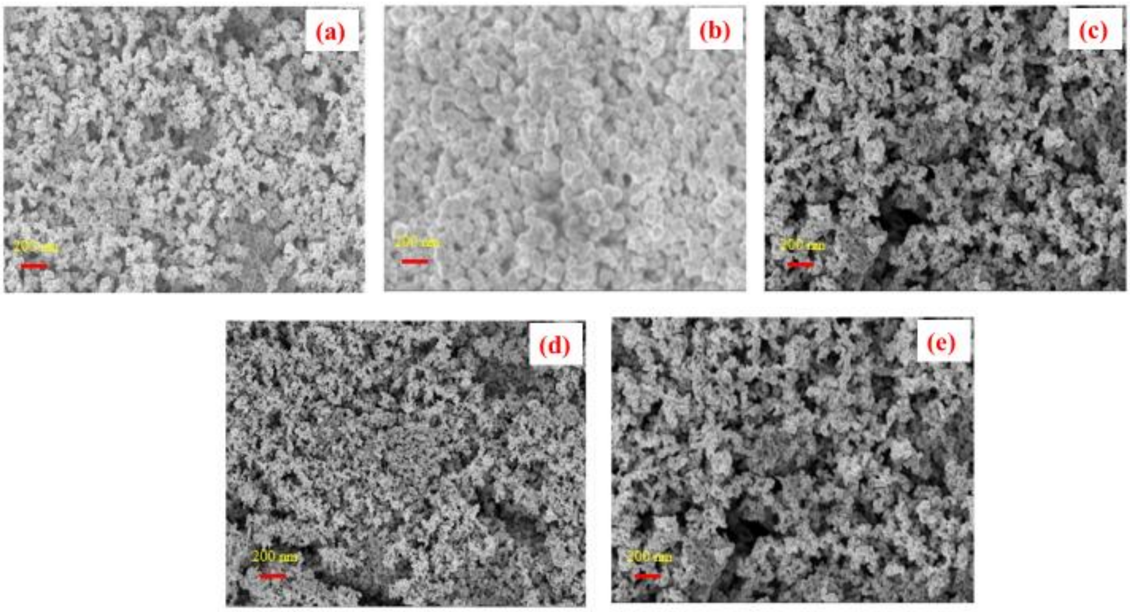

Figure 3.3 Typical FE-SEM images of as prepared $ZnSnO_3$ samples (a) S-01, (b) S-02, (c) S-03, (d) S-04 and (e) S-05.

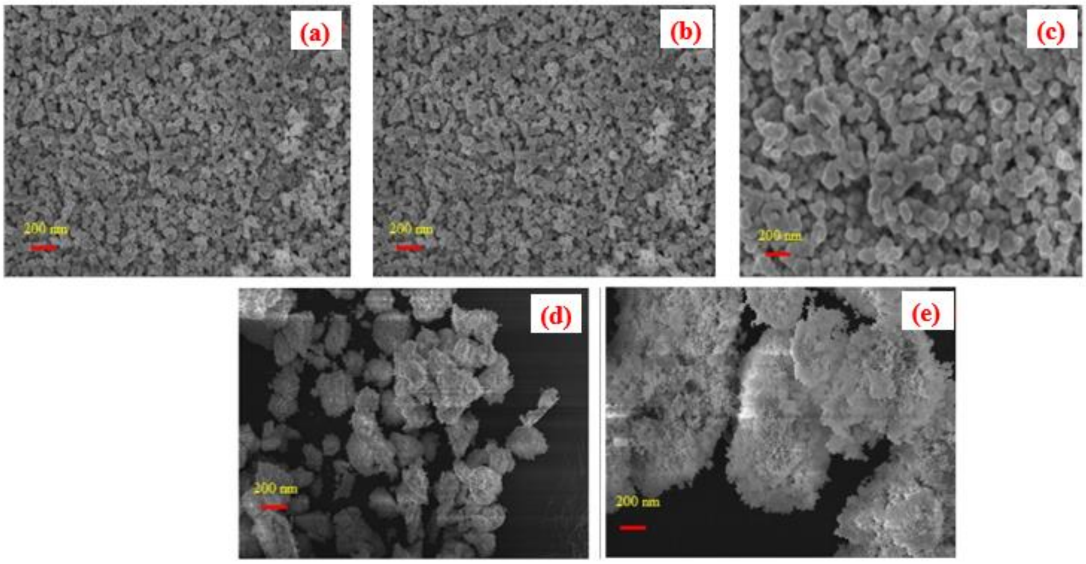

Figure 3.4 Typical FE-SEM images of 250˚C annealed $ZnSnO_3$ samples (a) S-01, (b) S-02, (c) S-03, (d) S-04 and (e) S-05.

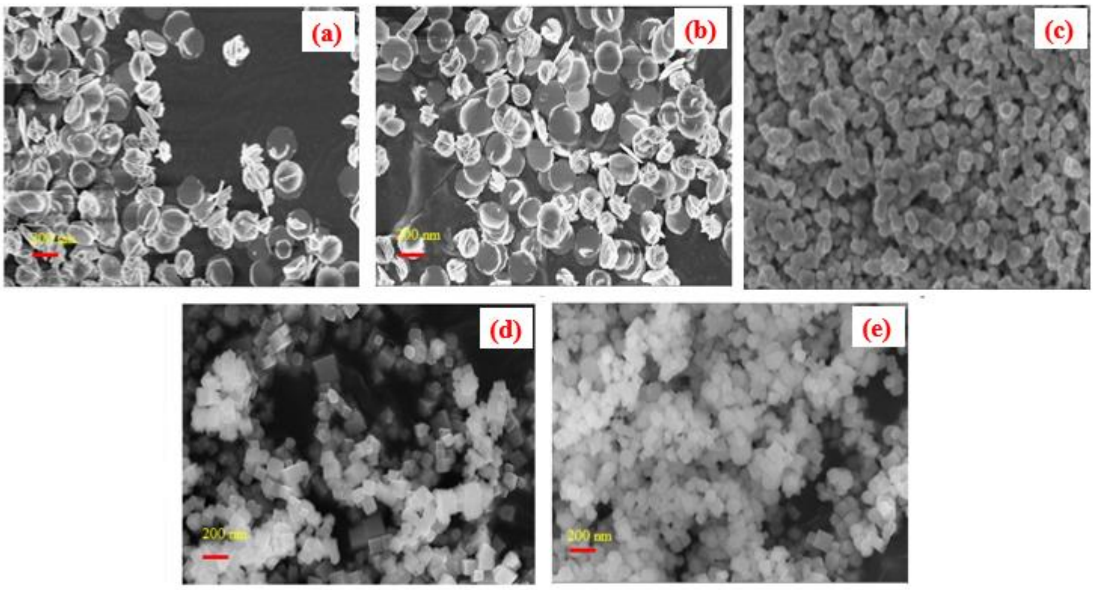

Figure 3.5 Typical FE-SEM images of 400˚C annealed $ZnSnO_3$ samples (a) S-01, (b) S-02, (c) S-03, (d) S-04 and (e) S-05.

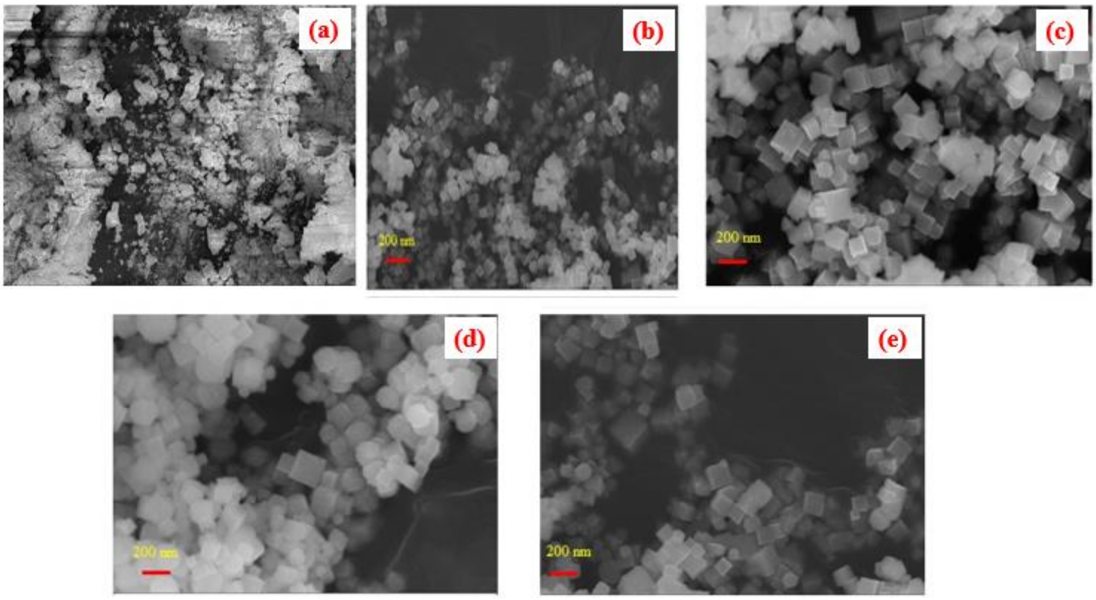

Figure 3.6 Typical FE-SEM images of 500˚C annealed ZnSnO3 samples (a) S-01, (b) S-02, (c) S-03, (d) S-04 and (e) S-05.

The FESEM analysis was used to identify the morphology of the synthesized $ZnSnO_3$ NP's. The SEM image of $ZnSnO_3$ nanoparticles shown in Fig. 3.3, reveals irregular morphology of the as-synthesized particles. The growth of zinc stannate nanoparticles is initiated by the reaction between zinc and tin ions during wet chemical synthesis. Whereas in Fig. 3.4 the 250°C annealed $ZnSnO_3$ samples shows partially developed regularity in morphology of moreover spherical nanoparticles. It has been observed that that for the samples S-04 and S-05, spherical particles and the formation of weak network of aggregates. The association of NP's can be ascribed to the annealing temperature where the spherical particles get associated to migrate into another morphology like cubes, flakes, sheets etc.

In Fig. 3.5, the FE-SEM images of 400°C annealed $ZnSnO_3$ samples were shown. It has been observed that 400°C annealed samples S-01, S-02 shows monodispersed homogeneous nanosheets type of morphologies with much higher thickness. Whereas from Fig. 3.5 (c-e), it was inferred that the morphology and size of cubes with nanometer sized particles were obtained in a periodic manner after heat treatment only. Smaller particles were observed at the surface of the micron sized particles, indicating that the particles are polycrystalline and self-organized from tiny crystallites.

The morphology shown in Fig.3.6 (a-e) shows well-nourished morphology from the as prepared samples of irregular shape to uniform cubic shapes with implementation of annealing temperature of 500°C, suggests the annealing effect over the $ZnSnO_3$ samples for their better sensing capacity. The cubic structures in Fig.3.6 generally have diameter of 85-100 nm, while the nanosheets shown in Fig.3.5 have average diameter of about 100nm.

The morphology of all the samples complied in Fig. 3.3-3.6 suggests a plausible growth mechanism of $ZnSnO_3$ crystallites. Here it can be predicted that the increase of stirring temperature and associated stirring time during the synthesis of zinc stannates helps the proper intermixing of Zn and Sn ions to come closer enough for the prominent growth of nanomaterials, which is also well nourished by applying an optimized heat treatment temperature following the Ostwald's ripening law governing such type of nanomaterials growth [20]. In comparison with other synthesis techniques, this adopted method of zinc stannate preparation has no external mechanism for guiding the growth of nanocubes, nanosheets etc. Hence the driving force for the anisotropic growth of the as prepared crystallites may derive from the inherent crystal structure of the materials and their chemical potential in solution. As in absence of any exact growth mechanism of cubic crystallites, here we assume the evolution of cubic particles is governed by a solution-solid (SS) process.

3.2.3. Thermogravimetric analysis (TGA) and Differential Thermogravimetric analysis(DTG):

Thermal analysis like TGA and DTG were conducted over the samples to determine the behaviour of the obtained $ZnSnSO_3$ nanomaterials towards applied temperature. TGA provides the physical or chemical properties (% wt. loss) of the material as a function of increasing temperature or time. Fig.3.3 shows the thermal analysis of dried powders before heat treatment. Thermal behavior of all the samples before annealing showed nearly 15- 16% weight loss up to 230 °C and from 230 to 900 °C almost 3% weight loss was observed.

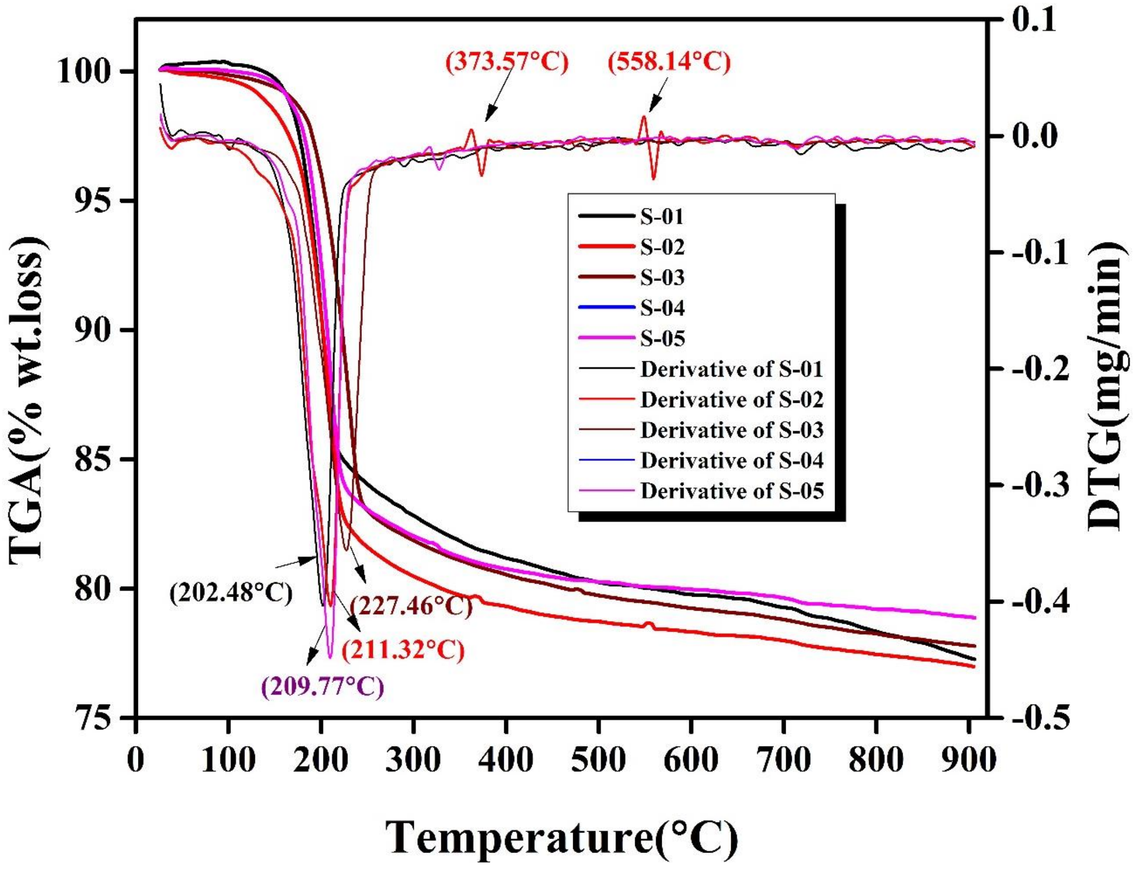

Figure 3.7 Thermogravimetric analysis (TGA) and Differential Thermogravimetric analysis(DTG) of as prepared $ZnSnO_3$ samples.

Thermal properties studied by TGA and DSC, as shown in Fig. 3.3, revealed the dehydration of water from the $ZnSnO_3$ exhibiting almost 15% weight loss in the sample near 250°C, justifies the disappearance of the -OH group. However, the water molecules trapped within the crystals require more energy (temperature) to remove than the surface water molecules, which can be seen later as another water dehydration peak between 230°C and 600°C, resulting in overall 19% reduction in the sample weight. The TG–DTG curves clearly show that the all prepared samples has one sharp weight loss step in the operating temperature range of 0–900 °C, as shown in Fig.3.3. The derivative thermogravimetric curve (DTG) was obtained through calculation. The TG–DTG curves exhibit a swift weight loss at the temperature range of 0–230 °C with endothermic peaks at 202.48°C, 211.32°C, 227.46°C and 209.77 °C, respectively for S-01, S-02, S-03 and both S-04 and S-05. This results from thermal analysis in form of endothermic peak in the DTG curve probably corresponds to the evaporation of the residual moisture. The chemical reaction equation can be expressed as follows:

$$ZnSnO_3.3H_2O \rightarrow ZnSnO_3 + 3H_2O$$

Along with the endothermic two much prominent exothermic peaks at about 373.57°C and 558.17ºC due to evolution loss of constitution lattice water and decomposition of more stable functional groups were also observed. With this an overall value of weight loss in the whole process is about 19.4-19.68%, is almost consistent with the theoretical value (19%) reported earlier.

3.2.4. BET and BJH Measurements:

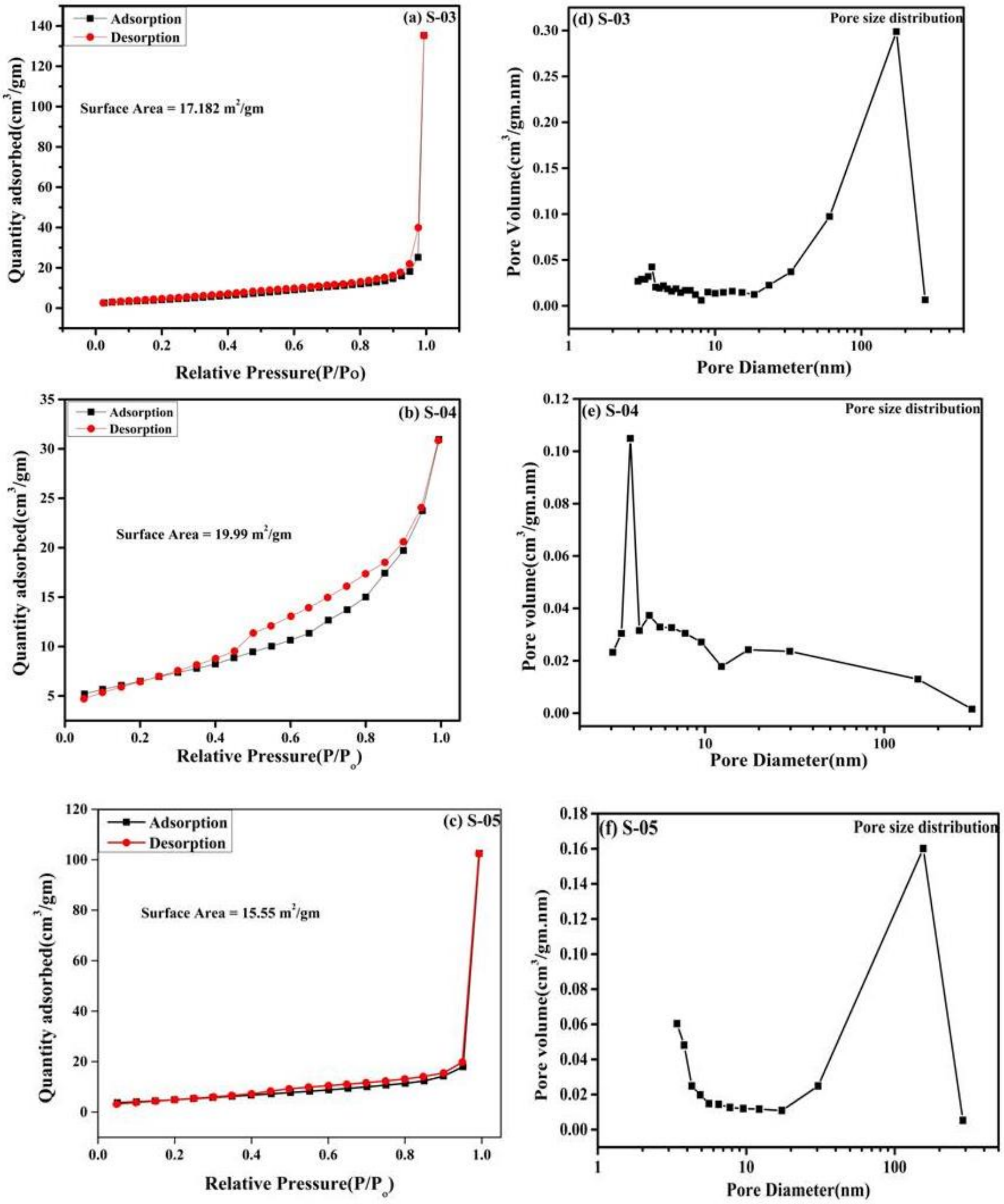

Figure 3.8 Adsorption- desorption isotherms of as prepared $ZnSnO_3$ samples (a) S-03, (b)S-04 and (c) S-05 and BJH pore size distribution of as prepared $ZnSnO_3$ samples (d) S-03, (e)S-04 and (f) S-05 respectively.

To further confirm the inner architectures of the porous $ZnSnO_3$ cubes, nitrogen adsorption and desorption measurements were performed to estimate the texture properties. The porous nature of $ZnSnO_3$ crystallites was studied by nitrogen adsorption-desorption isotherm measurements at 77 K. The adsorption-desorption isotherm can be categorized as type IV for S-04 sample which prepared by a maintained stirring temperature of 85°C suggesting the monolayer-multilayer adsorption and capillary condensation, hence the complete pore filling takes place increasing the surface area in comparison to other samples. This clearly indicates that the $ZnSnO_3$ sample with well-maintained growth parameters exhibits a large textural porosity. In case of S-03 and S-05 adsorption-desorption isotherm is categorized as type III suggests weak adsorptive-adsorbent interactions and incomplete pore filling. Brunauer-Emmett-Teller (BET) multipoint surface area of S-03, S-04 and S-05 measured that of 17.182 $m^2\ g^{-1}$, 19.99 $m^2\ g^{-1}$ and 15.55 $m^2\ g^{-1}$, respectively as shown in Fig.3.4 (a-c). The corresponding Barrett-Joyner-Halenda (BJH) pore size distribution for all the samples shown in Fig.3.4 (d-f) showed the pore size of 3.7 nm, 3.832nm and 3.412 nm respectively for S-03, S-04 and S-05. For all of the samples majority of the pores lie in the region of 5–50 nm suggesting all of them as mesoporous materials. The high surface area with advantageous mesoporous structure promotes enhanced humidity sensing properties due to faster protonic and electronic conduction over the material.

CHAPTER- 4

4. Result and Discussion

4.1. Device fabrication and Sensing Measurement

For sensor device fabrication, we used 1 cm x 1 cm ITO coated glass substrate as a substrate. A channel was made on this substrate by creating a scratch using a sharp diamond cutter as reported earlier in literatures, so that the two sides of the channel will act as source and drain. A channel length of 10 mm and width of 1mm was noted. A thick paste of as prepared and annealed samples of $ZnSnO_3$ individually was then drop-casted in the channel each time to prepare a no. of devices for carrying out set of experiments. This device was dried in furnace at 50ºC for 30 min and then used for the further sensing experiments. In order to obtain environments with a controlled level of humidity, the closed systems saturated with the vapor of the aqueous solutions of some known salts were used. The saturated aqueous solutions of KOH, $MgCl_2.6H_2O$, K_2CO_3, $Mg(NO_3)_2$, $NaNO_3$, NaCl, KCl, and K_2SO_4 in a closed glass container make up an environment with relative humidity of 8, 33, 43, 52, 63, 75, 86 and 97%, respectively [31-33]**.** These RH levels were monitored by a standard hygrometer (Comet Industries Pvt. Ltd.). The entire experiment was carried out at room temperature. For the sensing measurement, the prepared sensing devices were placed in the rubber sealed flask with a specific relative humidity (RH %) achieved from above stated saturated salt solutions at room temperature. The device under test (DUT) was mounted on to a rubber seal where two conducting wires with a portion firmly attached and were connected between the DUT and external power source (Keithley 2401 source meter). The DC electrical properties i.e., current-voltage (I-V) characteristics of $ZnSnO_3$ samples were measured with a voltage sweeping mode at various humidity points for checking the connection status.

The samples were noted as S-01, S-02, S-03, S-04 and S-05 in accordance to the stirring temperature at which they were synthesized i.e. at 25°C (Room Temperature), 45°C, 65°C, 85°C and 100°C. Also, other three sets of such samples were annealed at different temperature i.e.- 250˚C, 400˚C and 500˚C respectively to improve crystallinity and properties of all the four sets of samples were studied.

4.2. Sensitivity Test

For sensor response transient measurement, initially the biased DUT (Device Under Test) was kept in a container a fixed RH% (97 RH%), after the sensing response reached steady state, the biased DUT was quickly switched to another one at different RH%. The average switching time was kept short as to minimize possible interference in the transient response behaviour study. The humidity sensing analysis was done at relative humidity ranging from 8–97% helping towards deployment of the sensor over practical range of application.

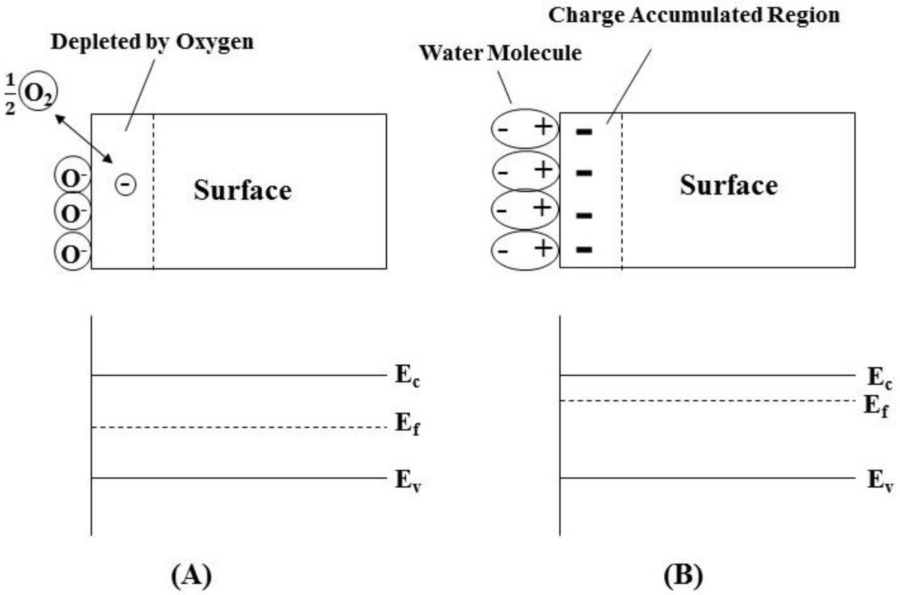

Figure 4.1 Schematic band diagram during humidity sensing. (A) In absence of water vapours the band position and charge distribution on the surface and (B) The shifting of fermi level by charge accumulation over the surface by donation of electron from the water vapours.

The humidity sensing is based on the mechanism of adsorption of water molecules on the surface of the material and proton conduction; the proton acts as an effective carrier for the electrical conductivity. The observed results imply that the H_2O molecules present in the saturated salts act as electron donors, resulting in an *n*-type doping. The water molecules present in the saturated salts adsorbed on the surface of $ZnSnO_3$ film shifts the Fermi level closer to the conduction band edge [5] as shown above in Fig. 4.1.

The plot between resistance and sensitivity *vs.* RH are shown in Fig.4.2- 4.5, which shows inverse relation between resistance and RH. The sensitivity $ZnSnO_3$ based humidity sensor were calculated using equation,

$$S(\%) = \frac{R_{08\%} - R_{\Delta R\%}}{R_{\Delta R\%}} \tag{4.1}$$

Where S (%) is sensitivity, $R_{08\%}$ and $R_{\Delta R\%}$ are the resistance of the device at lower humidity and after the change in humidity respectively**.**

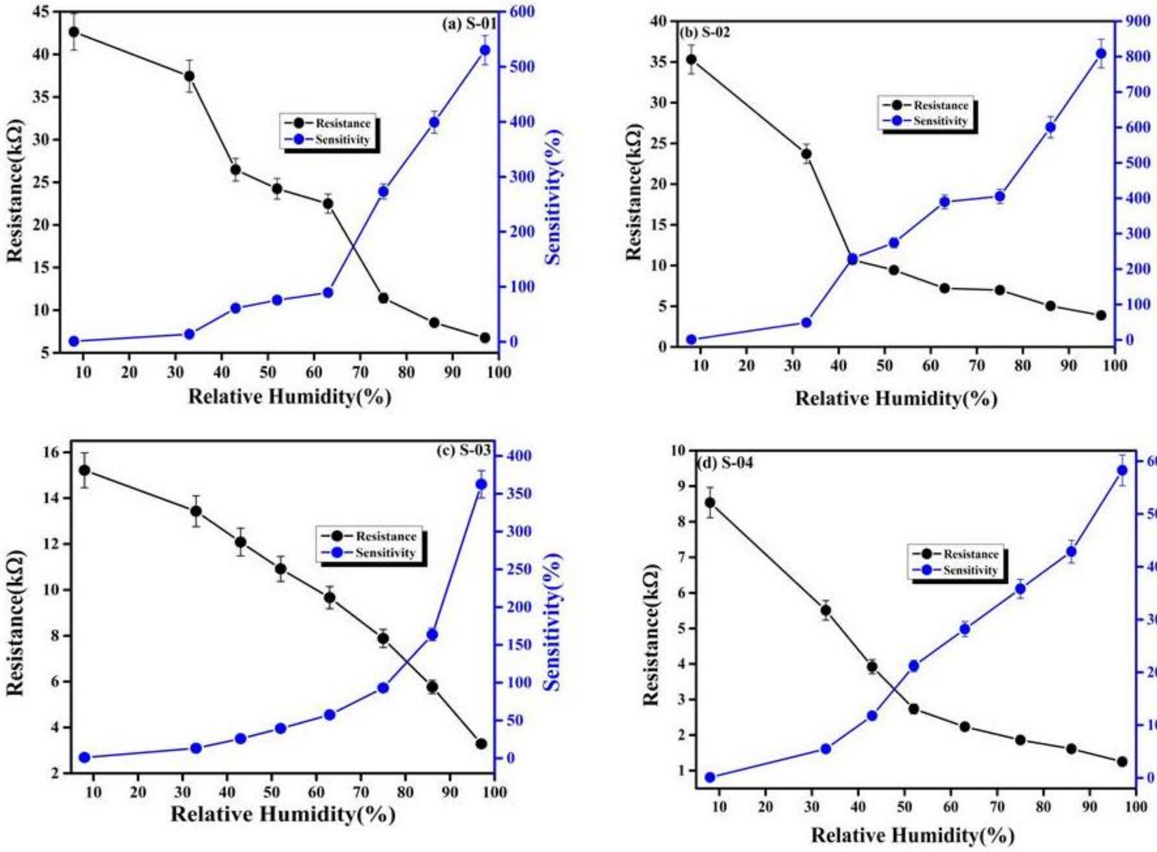

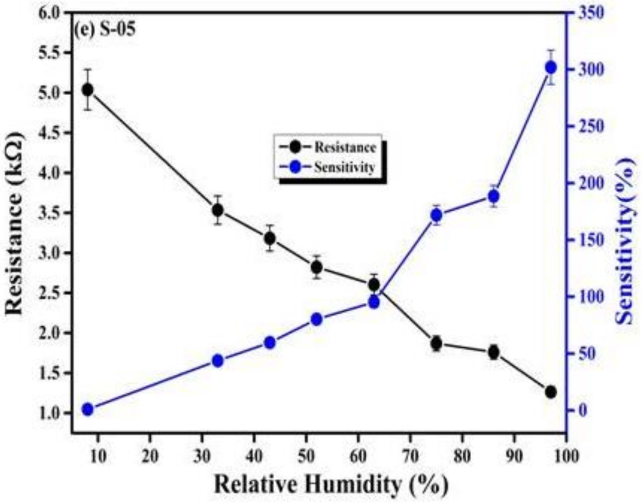

Figure 4.2 Typical plot of resistance and sensitivity vs. relative humidity for as prepared $ZnSnO_3$ samples (a) S-01, (b) S-02, (c) S-03, (d) S-04 and (e) S-05 based RH sensors.

According to equation (4.1) the sensitivity for all five as prepared $ZnSnO_3$ samples has been calculated and plotted along with its resistance for convenience. A constant decrease in resistance value for all the as prepared samples is observed at lowest RH value of 8% which comes around 42.63kΩ, 35.3kΩ, 15.21kΩ, 8.53 kΩ and 5.03kΩ for S-01, S-02, S-03, S-04 and S-05 respectively. The above stated resistance values go much lower extent to a value of 6.76kΩ, 3.88kΩ, 3.28kΩ,1.25kΩ and 1.26kΩ respectively for the samples in its chorological order of experimentation. Whereas no such trend was observed in case of the sensitivity factor for these samples. The sensitivity values came around 530.27%, 808.78%,362.59%, 582.74% and 301.92% for the samples starting from S-01 to S-05 respectively. The highest sensitivity of S-02 can be assumed for the optimum synthesis parameter controlled during the synthesis which helps to accommodate more humidity over the surface for better sensitivity.

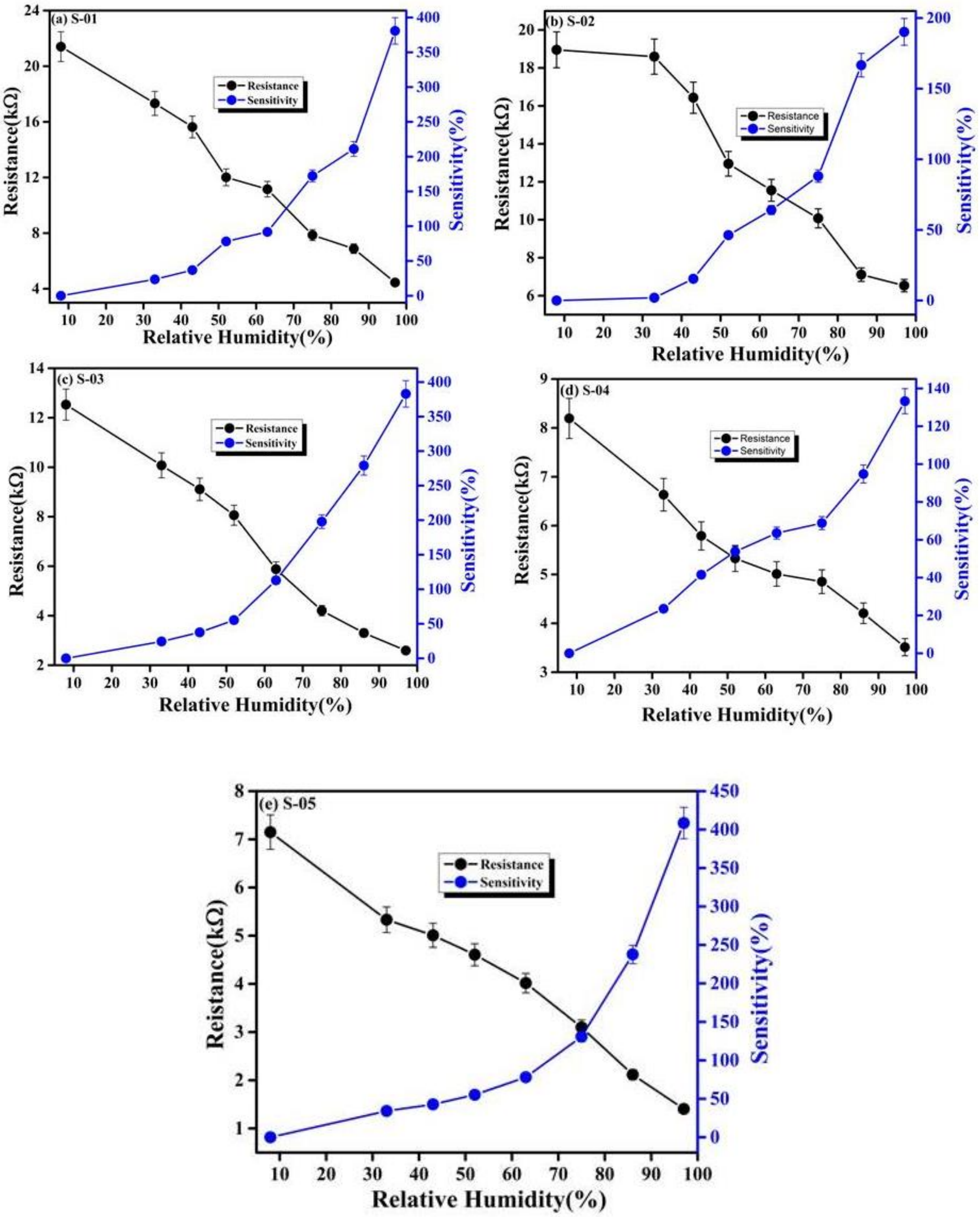

Figure 4.3 Typical plot of resistance and sensitivity vs. relative humidity for 250°C annealed (a) S-01, (b) S-02, (c) S-03, (d) S-04 and (e) S-05 $ZnSnO_3$ samples.

In continuation to the previous figure, the resistance and sensitivity of all the 250°C annealed zinc stannate samples are again plotted together for individual samples and assembled in Figure.4.3. Here also it has been observed that a constant decrease in resistance for all samples at lowest RH value of 8%. The resistance values at 8% RH were 21.40kΩ, 18.95kΩ, 12.53 kΩ, 8.194kΩ and 7.15kΩ whereas that at highest experimented RH value of 97% turned to be 4.45kΩ, 6.53kΩ, 2.595kΩ, 3.51kΩ and

1.4kΩ respectively for annealed samples noted as S-01, S-02, S-03, S-04 and S-05 respectively. In a similar condition stated as above here in these samples there was also no particular pattern of sensitivity decrease or increase.

The highest sensitivity obtained was 408.56% for 250° annealed S-05 sample by transferring the sample from 8% to 97% RH chamber. The other sensitivity factor obtained for the other annealed samples were 380.79%, 190.18%,382.92% and 133.26% for S-01, S-02, S-03 and S-04 respectively.

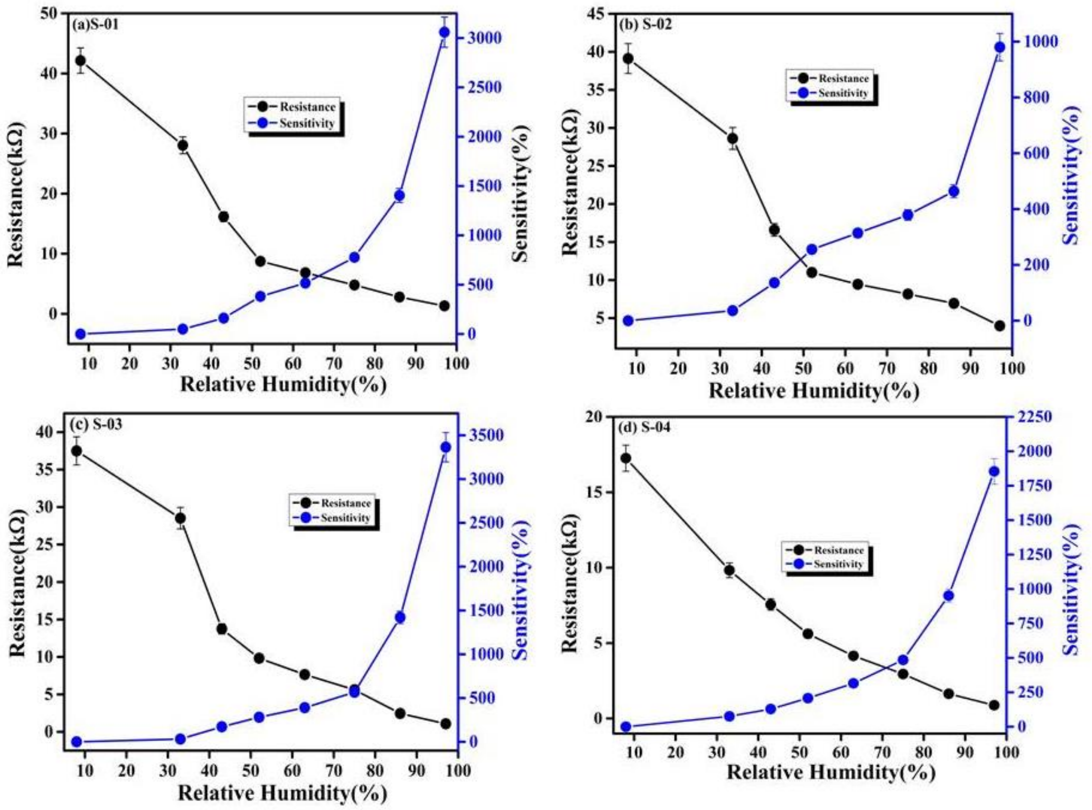

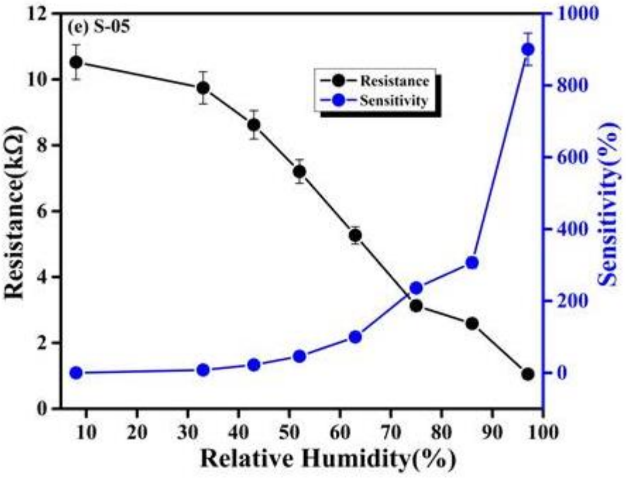

Figure 4.4 Typical plot of resistance and sensitivity vs. relative humidity for 400°C annealed (a) S-01, (b) S-02, (c) S-03, (d) S-04 and (e) S-05 $ZnSnO_3$ samples.

Here in Figure 4.4 the resistance and sensitivity against % Relative Humidity for all 400°C annealed $ZnSnO_3$ samples were assembled. The individual plot elaborates the relation between sensitivity and resistance of samples. From the Fig.4.4 it is observed that a continuous decrease in sample resistance at lowest experimented RH value of 8% which comes around 42.15kΩ, 39.12kΩ, 37.49kΩ,17.25kΩ and 10.52kΩ for 400°C annealed S-01, S-02, S-03, S-04 and S-05 samples respectively.

This resistance value at lowest relative humidity goes further down to an extent of 1.33kΩ, 3.99kΩ, 1.08kΩ, 0.88kΩ and 1.05kΩ respectively for the samples by placing it at 97% relative humidity chamber. The continuous decrease in resistance can be ascertained to the annealing temperature effect which plays a secondary role after the synthesis temperature. Again, sensitivity factor of samples was determined using equation (4.1) and this comes around 3059.93%, 980.36%, 3364.45%,1854.15% and 900.64% respectively for samples ranging S-01 to S-05. The higher sensitivity is in correlation with N_2 adsorption-desorption isotherm study suggesting mesoporous materials are better sensor materials for much specific practical utility.

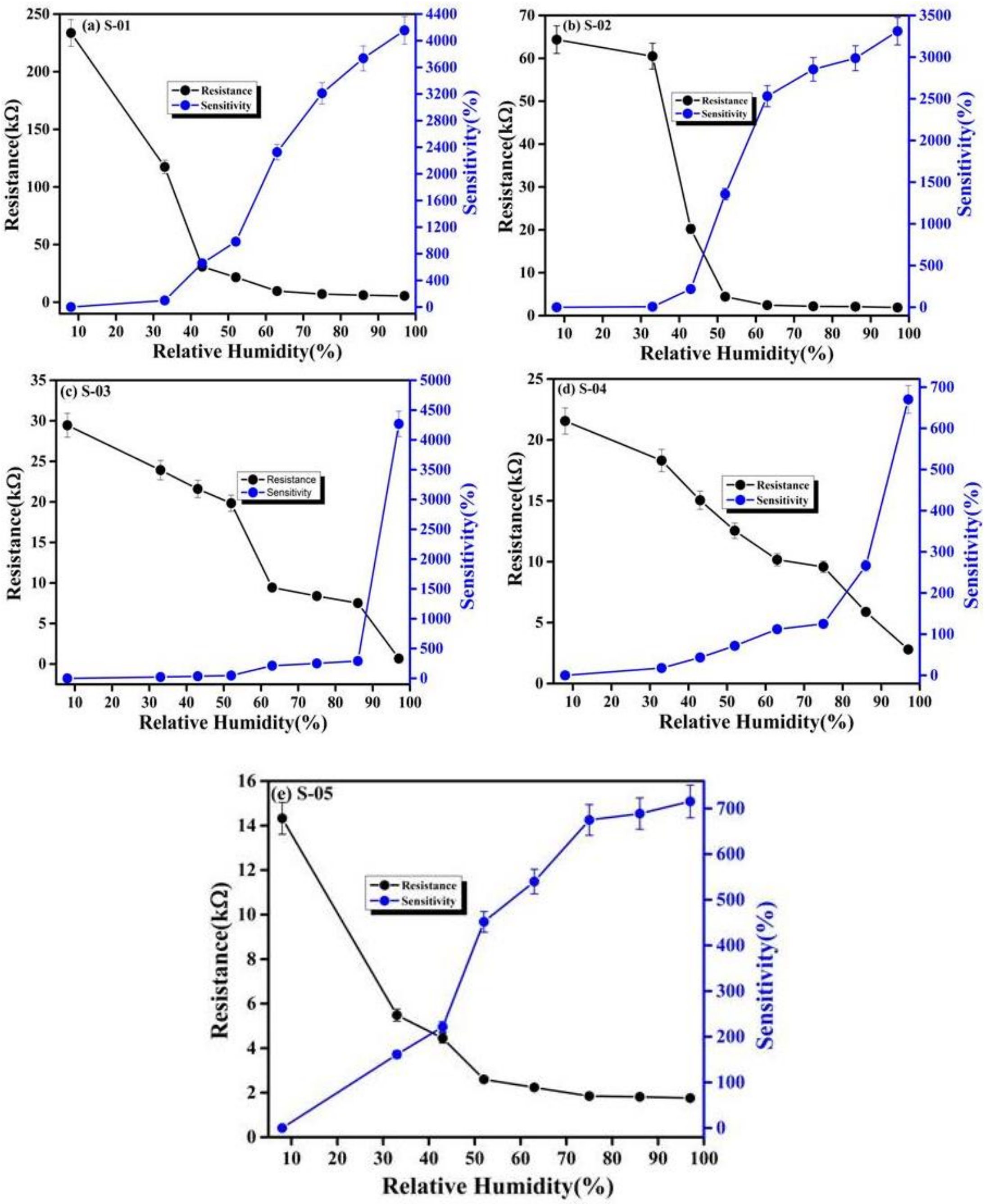

Figure 4.5. Typical plot of resistance and sensitivity vs. relative humidity for 500°C annealed (a) S-01, (b) S-02, (c) S-03, (d) S-04 and (e) S-05 $ZnSnO_3$ samples.

Figure 4.5 shows variation of sensitivity factor and resistance as a function of relative humidity of 500°C annealed $ZnSnO_3$ samples. The resistance value for samples at 8% RH were 233.64 kΩ, 64.36kΩ, 29.45kΩ, 21.55kΩ and 14.32 kΩ respectively and which goes further down to a value of 5.49kΩ, 1.88kΩ, 0.67kΩ, 2.79kΩ and 1.75kΩ respectively at relative humidity of 97% in a closed chamber. When we consider the sensitivity change at the same condition i.e. within a transition range of 8%-97% relative humidity the values turned as 4155.77%, 3310.73%,4268.91%,670.34% and 715.44% respectively for samples denoted as S-01, S-02, S-03, S-04 and S-05. The comparison of sensitivity factor of all the as prepared and annealed samples indicates that 500°C samples are acting as better humidity sensors. All the prepared $ZnSnO_3$ samples after annealing shows a periodic decrease in resistance values along with a marginal continuation in sensitivity factor with increase in %RH establishes the potential sensing performance.

4.3. Hysteresis Study of Humidity Sensors

The humidity sensor is one of the important applications of proton-conducting solid electrolytes. Generally, the principle of humidity sensors is based on the change of capacitance or conductance of a solid due to the adsorption of water vapor. Many fast-proton conductors are solid hydrates, which show varying degrees of protonic conduction at different humidity levels. This makes $ZnSnO_3$ type perovskite materials a strong candidate for developing humidity sensors at room temperature. In order to show the hysteresis of the sensor device, the resistance through the device was measured at various humidity levels (with increasing humidity from 8% to 97% and then decreasing it back to 8%).When the RH decreases from 97% to 8% and then increases again from 8% to 97%, the output resistance of the sensor drifts from the initial value at the same RH, which defines the hysteresis. The hysteresis is probably caused by the different rates of adsorption and desorption of water vapours. The humidity hysteresis of the sensor based on as prepared and different temperature annealed i.e. 250°C, 400°C and 500°C annealed $ZnSnO_3$ samples was shown in Fig.4.6-4.9. The humidity sensors usually exhibit a hysteresis error (Shown in Table 4.1-4.4) calculated as the difference in the sensor resistance during the process of uptake and release of water molecules. The expression,

$$\mathrm{H_e} = \pm \frac{\Delta H_{max}}{2F_{FS}} \tag{4.2}$$

is used to calculate the hysteresis error (H_e), where the ΔH_{max} is the difference in the output for the process of adsorption and desorption and F_{FS} is the full-scale output [22]. As observed in Fig.4.6-4.9, the curves of adsorption and desorption for the different $ZnSnO_3$ humidity sensors nearly superimpose each other at higher %RH value. The hysteresis study inferred that the comparative lowering in hysteresis for 400°C and 500°C annealed $ZnSnO_3$ samples than as synthesized and 250°C annealed sample has more practical viability for its use in electronic device applications as minimizing the hysteresis effect is crucial for practical sensing application. From the Table 4.1, it can be seen that the hysteresis values are quite small for most of the humidity levels which is significantly less than the earlier reported results [23].

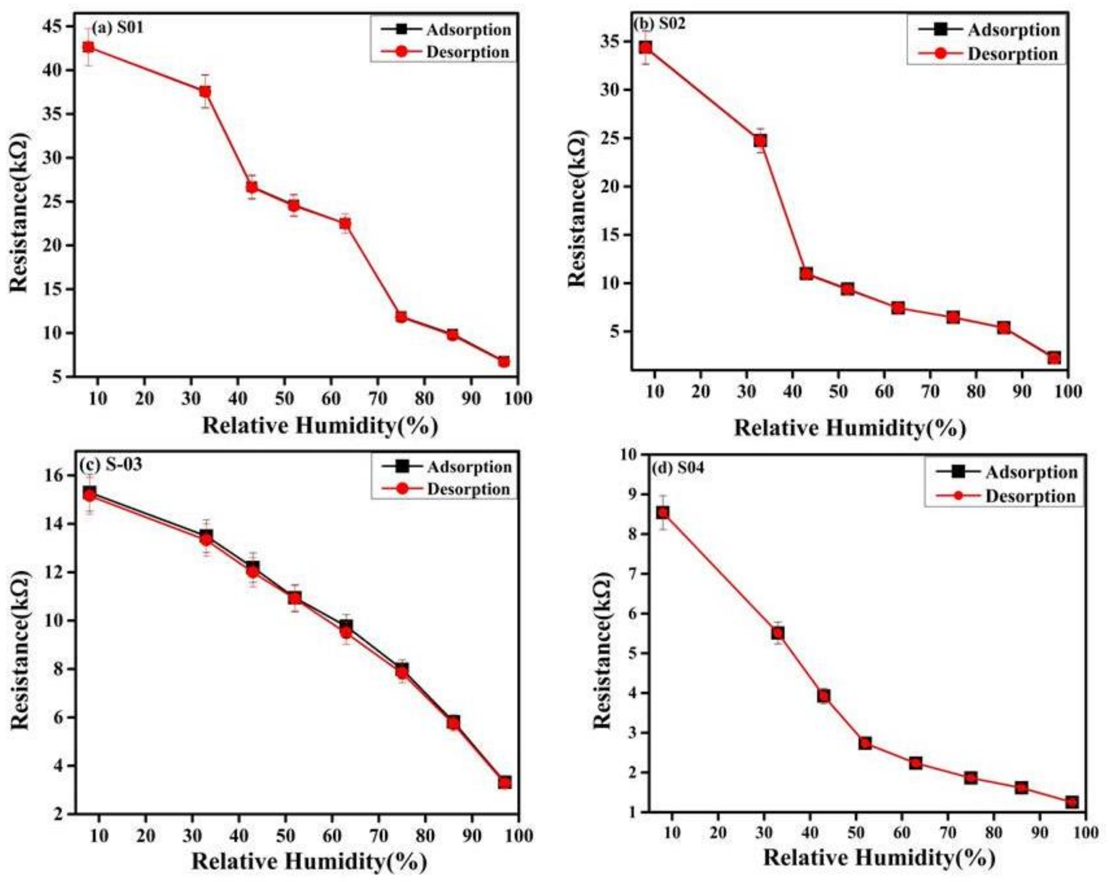

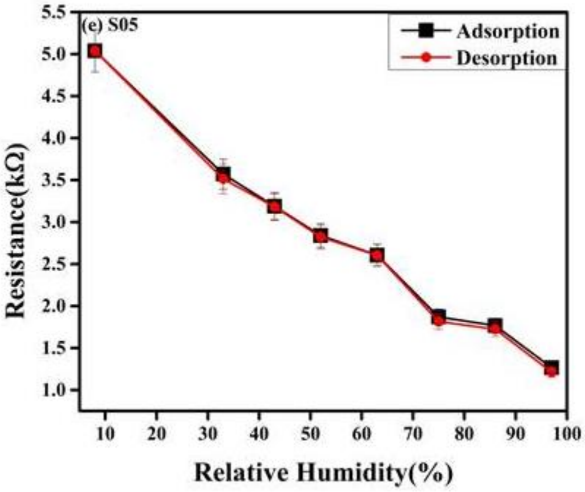

Figure 4.6 Typical hysteresis characteristics of the as prepared (a) S-01, (b) S-02, (c) S-03, (d) S-04 and (e) S-05 $ZnSnO_3$ samples.

During the whole adsorption-desorption process, the maximum absolute value of H_e obtained was 0.00195 at 43% RH for S-01, 0.01108 at 52% RH for S-02, 0.00649 at 33% RH for S-03, 0.00448 at 52% RH for S-04 and 0.01413 at 86% RH for S-05 within 08-97% RH change for as prepared $ZnSnO_3$ samples with a better reliability of the sensors.

Table 4.1 Hysteresis values at different levels of RH for as prepared $ZnSnO_3$ samples.

% RH	S-01	S02	S03	S04	S05
	H_e	H_e	H_e	H_e	H_e
8	0.00018	0.00065	0.00118	0.00035	0.01115
33	0.00029	0.00740	0.00649	0.00177	0.00368
43	0.00195	0.00583	0.00365	0.00011	0.00565
52	0.00003	0.01108	0.00264	0.00448	0.00918
63	0.00019	0.00011	0.00324	0.00177	0.00224
75	0.00002	0.00494	0.00296	0.00289	0.00002
86	0.00004	0.00294	0.00454	0.00028	0.01413
97	0.00003	0.00145	0.00004	0.00100	0.00807

The results in Table 4.1 pointed out that the highest hysteresis error obtained lies in the low RH regime (0-50% RH) focuses a marked physical change dependent over the water uptake by the material.

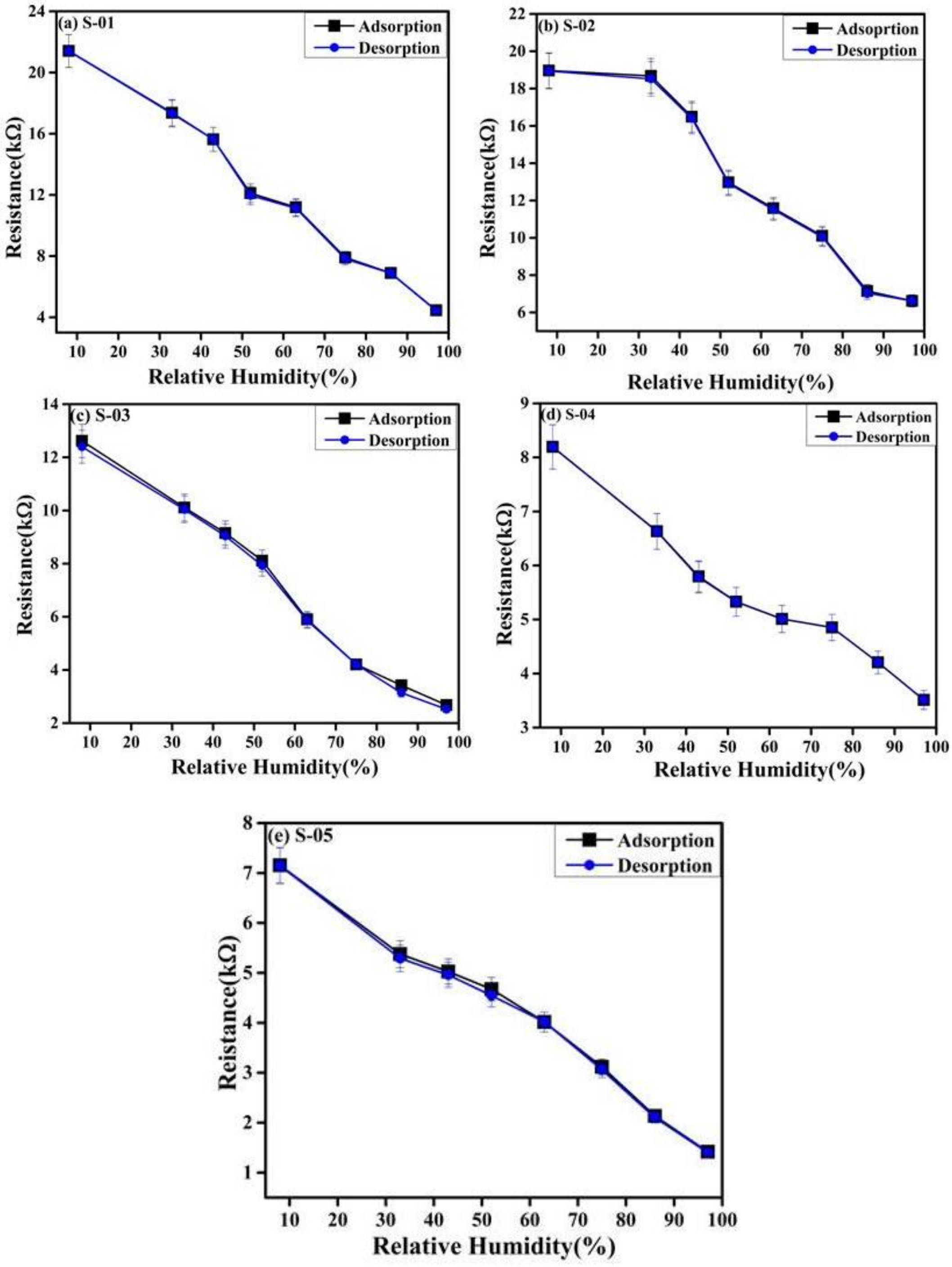

Figure 4.7 Typical hysteresis characteristics of 250°C annealed (a) S-01, (b) S-02, (c) S-03, (d) S-04 and (e) S-05 $ZnSnO_3$ samples.

Table 4.2 constitutes the hysteresis error values for all the $ZnSnO_3$ samples annealed at 250°C at every RH value within 08-97% RH range. During the whole adsorption-desorption process, the maximum absolute value of H_e obtained was 0.01165 at 63% RH for S-01, 0.00743 at 33% RH for S-02, 0.00178 at 86% RH for S-03, 0.0013 at 86%

RH for S-04 and 0.000137 at 33% RH for S-05 within 08-97% relative humidity range for the corresponding annealed $ZnSnO_3$ samples.

Table 4.2 Hysteresis values at different levels of RH for 250°C annealed $ZnSnO_3$ samples.

% RH	S-01	S02	S03	S04	S05
	H_e	H_e	H_e	H_e	H_e
8	0.00558	0.00027	0.00001	0.00096	0.00000068
33	0.00688	0.00743	0.00081	0.00070	0.00014
43	0.00830	0.00099	0.00099	0.00111	0.00014
52	0.00159	0.00233	0.00139	0.00096	0.00007
63	0.01165	0.00031	0.00000	0.00000	0.00001
75	0.00662	0.00714	0.00096	0.00039	0.00000
86	0.00381	0.00550	0.00178	0.00038	0.00023
97	0.00189	0.00675	9.83E-04	0.0013	0.000000686

It has been observed that even for the sample S-05 all the hysteresis error values were placed after fourth place decimal value which provides too negligible hysteresis error during interfacing these materials for practical humidity sensor with better performance.

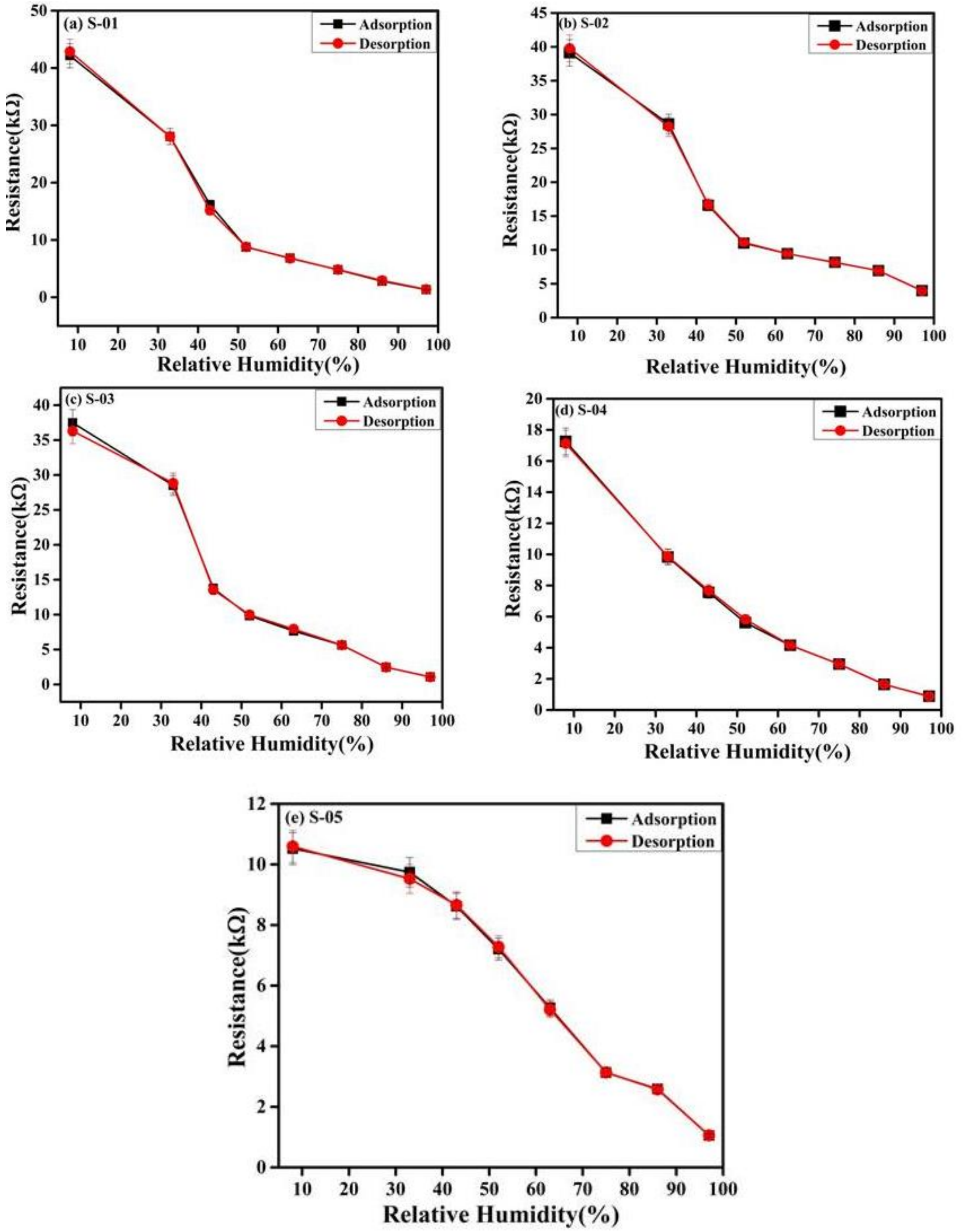

Figure 4.8 Typical hysteresis characteristics of 400°C annealed (a) S-01, (b) S-02, (c) S-03, (d) S-04 and (e) S-05 $ZnSnO_3$ samples.

Table 4.3 constitutes the hysteresis error values for all the $ZnSnO_3$ samples annealed at 400°C at every RH value within 08-97% RH range. During the reversible process, it has been observed that the hysteresis values at high RH regime fall in 10^{-4} order indicating the lowering of practical error for real life application of the $ZnSnO_3$ material as humidity sensor. The maximum absolute value of H_e obtained for these samples were 0.0096 at 8% RH for S-01, 0.00448 at 33% RH for S-02, 0.01218 at 43% RH for S-03, 0.01155 at 33% RH for S-04 and 0.00667 at 52% RH for S-05.

Table 4.3 Hysteresis values at different levels of RH for 400°C annealed $ZnSnO_3$ samples.

% RH	S-01	S02	S03	S04	S05
	H_e	H_e	H_e	H_e	H_e
8	0.00960	0.01657	0.00876	0.00383	0.00419
33	0.00587	0.00448	0.00015	0.01155	0.00112
43	0.00203	0.00267	0.01218	0.00204	0.00389
52	0.00169	0.00211	0.00057	0.00401	0.00667
63	0.00002	0.00413	0.00065	0.00285	0.00027
75	0.00043	0.00026	0.00049	0.00034	0.00003
86	0.00014	0.00002	0.00171	0.00088	0.00030
97	0.000526	0.000275	0.000678	0.000451	0.000277

Table 4.4 comprises the hysteresis error value of all $ZnSnO_3$ samples annealed at 500°C. At a first instance, it has been clearly observed that the hysteresis error for all the samples goes much lower and practically there will be no significant effect of it over device assembly and implementation. The highest hysteresis error value achieved during the adsorption-desorption process comes around 0.000149 at 63% RH for S-01, 0.00773 at 63% RH for S-02, 0.00015 at 33% RH for S-03, 0.01222 at 52% RH for S-04 and 0.01031 at 8% RH for S-05.

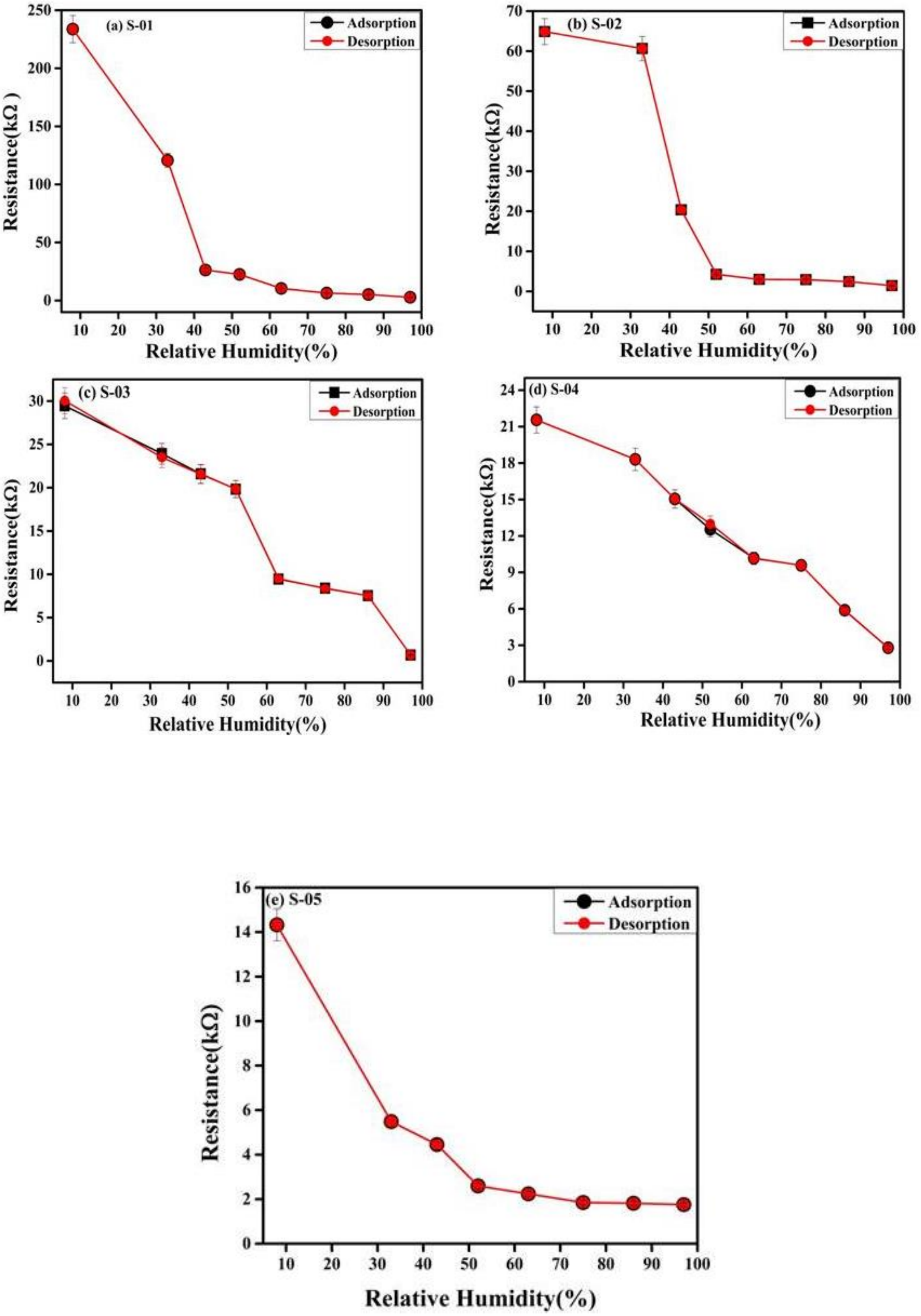

Figure 4.9 Typical hysteresis characteristics of 500°C annealed (a) S-01, (b) S-02, (c) S-03, (d) S-04 and (e) S-05 $ZnSnO_3$ samples.

Table 4.4 Hysteresis values at different levels of RH for 500°C annealed $ZnSnO_3$ samples.

% RH	S-01	S02	S03	S04	S05
	H_e	H_e	H_e	H_e	H_e
8	0.000012	0.000001	0.000002	0.000095	0.010310
33	0.000390	0.002820	0.000150	0.000067	0.007400
43	0.000005	0.004520	0.000164	0.000219	0.000634
52	0.000017	0.000280	0.000080	0.012220	0.000246
63	0.000149	0.007300	0.000070	0.000510	0.000849
75	0.000059	0.001140	0.000168	0.000025	0.000660
86	0.000002	0.000300	0.000013	0.000488	0.000279
97	0.0000095	0.00000189	0.0000529	0.000503	0.00000305

4.4. Relative Deviation in Resistance and Freundlich Isotherm Behaviour

Isotherm models like Freundlich model were utilized to explain the relationship between sensing data within a RH range when applied for modelling of vapor adsorption and the available plausible mechanism of humidity sensing. In case of humidity sensing hydrogen bonding between adsorbed water molecules with surface active groups occur, on and within the nanostructure as surface interactions accounting for the reversibility of water adsorption-desorption process. In general, the Freundlich isotherm curve relates the concentrations of solute on the surface of an adsorbent (oxygen on the surface of experimented sample) and the solute concentration (water vapor).The relationship between S (relative deviation in resistance) and C (percent relative humidity) can be expressed as, $S= k.C^{\alpha}$ where k and α are the proportionality and exponent constants and represent the adsorption capacity and adsorption intensification or strength respectively[24, 25, 26]. To our knowledge, this is the first attempt of this kind to apply the Freundlich adsorption model to the uptake of water vapours on metal stannate based humidity sensors.

Relative deviation in resistance (ΔR_H) is an important factor describing the resistance variation during switching between different RH environments for practical interfacing of any device. From Fig.4.10-4.13, on minute observation it is observed that as prepared and annealed $ZnSnO_3$ humidity sensor samples show two significant regions when plotted against relative humidity. The existence of these two regions is related to the conduction mechanism where region before and after transition point (T_c) was ascribed to conduction through chemisorbed layers and physisorbed layers respectively. In order to exemplify this transition behaviour, Freundlich adsorption isotherm model is considered for the respective sensor samples. The slope of the graphs of RDR against % RH in two regions is different. Therefore, while interfacing these sensors to the electronic circuit and during calibration of devices, the two regions must be separately considered hence lowering in T_c value improves practical applicability during interfacing and monitoring.

Relative deviation in Resistance (R.D.R) is best known practical aspect which should be taken care of before going for any device sort of application of any sensing material. Here the values of relative deviation in resistance (R.D.R) in % is calculated for all of samples under study by using expression and plotted against relative humidity (%RH)

$$\Delta \mathrm{R_H} = (\mathrm{R_{LH}} - \mathrm{R_H}) / \mathrm{R_{LH}} \times 100\% \qquad (4.3)$$

The R_{LH} is the resistance of the sample measured at lower humidity (RH = 8% RH) and R_H is the resistance of the samples at any humidity in RH%. From Fig.4.10-4.13, it is noticed that, the values of RDR (%) increases with increase in the relative humidity. As shown in Figure 4.10 (a) within the range of investigation, the variation in RDR extended up to 84.1%, 89%, 78%, 85% and 75% respectively for the as prepared $ZnSnO_3$ samples noted as S-01 to S-05 without annealing from the initial value respectively. Even a coexistence of two different regions is marked in the extended relative humidity range. The existence of these two regions can be attributed to the conduction mechanism.

The Fig.4.10 (b-f) shows the experimental water adsorption data plotted in the linear format of the Freundlich model with two distinct linear regions within entire RH range. The two linear regions associated to two different adsorption regimes, one at lower RH values (5%-52%) and another one at higher RH values (52%-97%). The transition point

(T_c) was determined by calculating the point where the two linear fits cross each other. The result indicates a significant variation between two different adsorption regimes for all five samples. The linear fitting of two regions were done separately in accordance to Freundlich model, and the Freundlich constants, *k* and *α*, were determined and presented in Table 4.5 for both adsorption regimes of as prepared $ZnSnO_3$ samples. Previous studies remarked that adsorption intensification (*α*) value greater than unity indicates strong adsorption behaviour. [24]

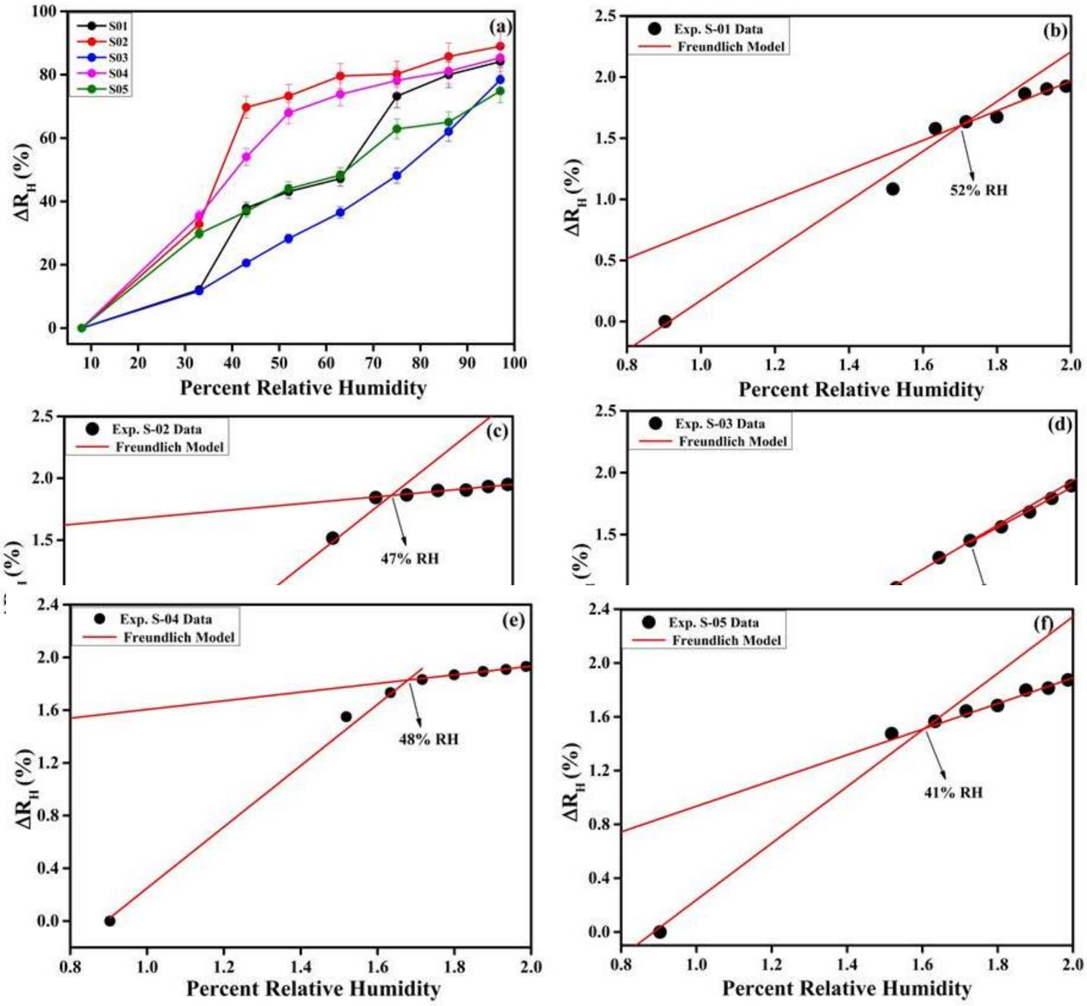

Figure 4.10 Log-Log plot of (a) measured Relative Deviation in resistance (ΔRH) vs. percent relative humidity of as prepared samples and individually modelled (Freundlich) behaviour of measured R.D.R vs. percent relative humidity for (b) S-01 (c) S-02, (d) S-03, (e)S-04 and (f) S-05 $ZnSnO_3$ samples.

As shown in Table 4.5, the value α for all samples is nearly above unity within low RH range (5%-52%), indicating that all the $ZnSnO_3$ nanostructures have a strong affinity for water vapor. But this value increases from 1.20958 to 2.32455 by changing the sequence from S-01 to S-04 and suddenly it decreases down to 0.99431(~1) for S-05 indicates the decrement in water affinity.

Table 4.5 Results from Freundlich Adsorption Model including the Adsorption Capacity (k), Adsorption Strength (α), R^2 value on humidity sensing of as prepared $ZnSnO_3$ samples.

Sample No.	Low RH Regime			High RH Regime		
	k	α	R^2	k	α	R^2
1	2.83 ±0.38	1.20 ±0.20	0.89269	7.24 ±0.30	2.03 ±0.20	0.96978
2	2.52 ±0.12	1.27 ±0.06	0.83905	1.39 ±0.21	2.39 ±0.12	0.98939
3	2.37 ±0.13	1.63 ±0.07	0.99214	1.45 ±0.04	1.78 ±0.03	0.99902
4	1.18 ±0.20	2.32 ±0.14	0.98893	1.89 ±0.03	0.32 ±0.01	0.99
5	1.04 ±0.33	0.99 ±0.17	0.90565	7.37 ±0.29	2.10 ±0.19	0.97349

Conversely, in the high RH regimes, the α value doesn't show any particular pattern of increase or decrease. Although the value got increased from 2.03 to 2.39 by going to S-01 to S-02 and then suddenly decreased down to 1.78 and 0.32 for S-03 and S-04 respectively. Again, it got increased in case of S-05 to the α value of 2.1. This randomness in α value for all samples, indicates a weaker adsorption regime at higher RH values in comparison to smooth adsorption intensification for the samples at lower RH regime. The significant 'α' value for S-03 hints towards the increase in no. of surface active sites for adsorption-desorption process which decreases further for the next samples which synthesized at higher stirring temperature making it one of the potential as synthesized stannate materials for humidity sensor. The calculated k value represents the water adsorption capacity at particular RH state. In the low RH regime, the $ZnSnO_3$ samples showed a clear decrease in the value starting from 2.83 to 1.04 for S-01 to S-05 followed by 2.52(S-02), 2.37(S-03) and 1.18(S-04). Whereas in the high RH regime, we find k values for the S-01 is 7.24 which suddenly decreases down to 1.39(S-02), 1.45 (S-03) and 1.89(S-04) and again at an instant it increases to an extent k value of 7.37 for S-05 indicating a marked deviation in the trend of adsorption capacities as that of in low RH regime.

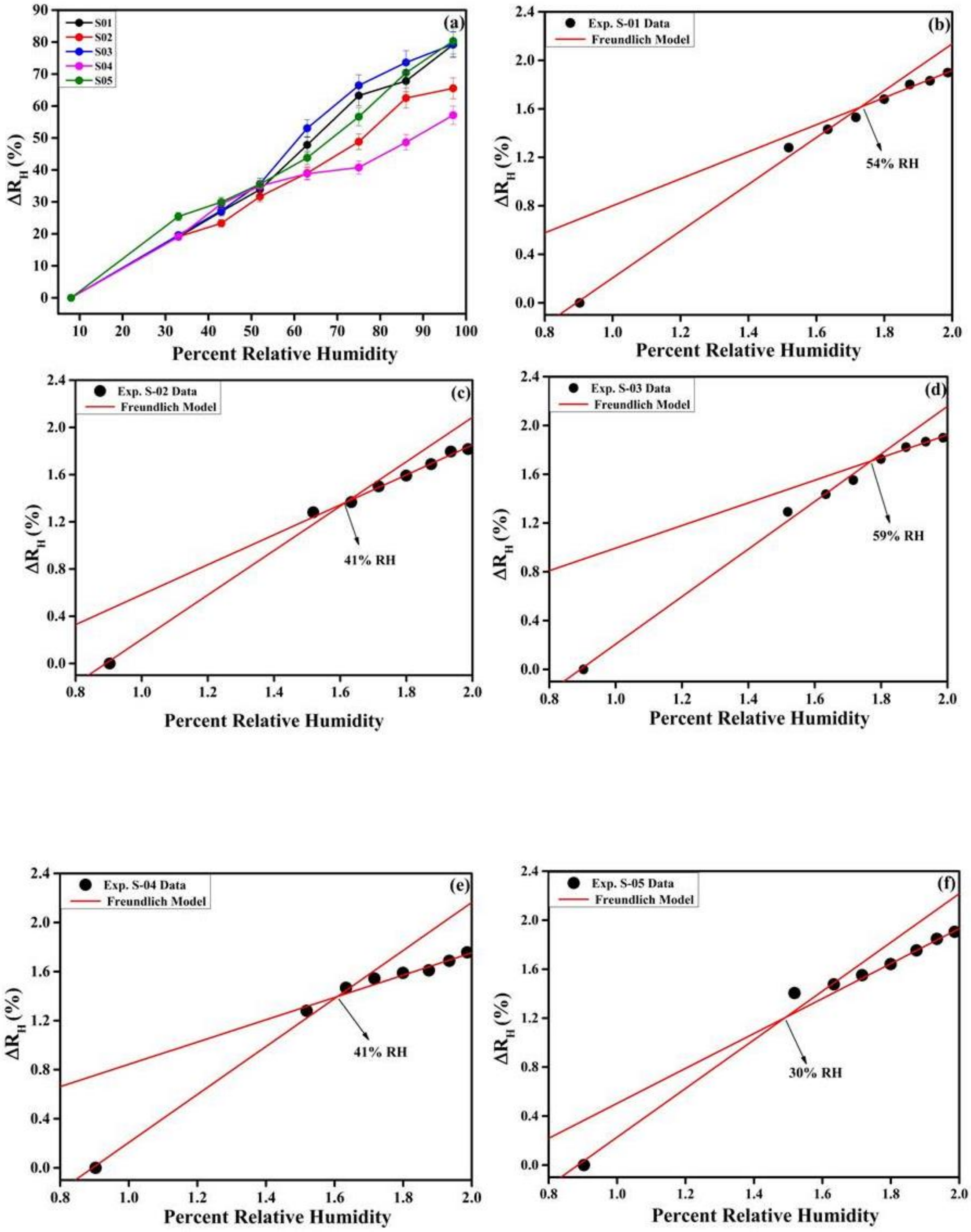

Figure 4.11 Log-Log plot of (a) measured Relative Deviation in resistance (ΔRH) vs. percent relative humidity of 250°C annealed $ZnSnO_3$ samples and individually modelled (Freundlich) behaviour of measured R.D.R vs. percent relative humidity for (b) S-01, (c) S-02, (d) S-03, (e) S-04 and (f) S-05 250°C annealed $ZnSnO_3$ samples.

As shown in Figure 4.11 (a) within the range of investigation, the variation in RDR extended up to 79.2%, 65.5%, 79.3%, 57.1% and 80.3% respectively for the 250°C annealed $ZnSnO_3$ samples noted through S-01 to S-05 from its initial resistance value respectively.

Table 4.6 Results from Freundlich Adsorption Model including the Adsorption Capacity (*k*), Adsorption Strength (*α*), R^2 value on humidity sensing of 250°C annealed $ZnSnO_3$ samples.

Sample No.	Low RH Regime			High RH Regime		
	k	α	R^2	k	α	R^2
1	2.06 ±0.28	1.11 ±0.15	0.94715	5.31 ±0.15	1.93 ±0.10	0.99109
2	4.85 ±0.32	1.26 ±0.17	0.9477	4.76 ±0.19	1.88 ±0.13	0.98552
3	1.16 ±0.22	0.92 ±0.11	0.95393	5.54 ±0.15	1.95 ±0.10	0.9919
4	1.16 ±0.37	0.90 ±0.19	0.87289	5.63 ±0.14	1.95 ±0.10	0.99207
5	8.39 ±0.12	1.42 ±0.06	0.99389	5.78 ±0.29	1.98 ±0.20	0.97009

This clearly indicates that S-04 shows the lowest deviation at highest 97% RH value put forward it as most suitable candidate for next generation humidity sensor.

The Fig.4.11 (b-f) shows the experimental water adsorption data plotted for individual 250°C annealed sample in the linear format of the Freundlich model with two distinct linear regions within entire RH range. The two linear regions associated to two different adsorption regimes, one at lower RH values (5%-52%) and another one at higher RH values (52%-97%). The transition point (T_c) was determined by calculating the point where the two linear fits cross each other. The result indicates a significant variation between two different adsorption regimes for all five samples. The transition point (T_c) for the samples were found to be 54%, 41%, 59%, 41% and 30% for samples S-01 followed through S-05 respectively. The lowering of T_c value confirms the increasing applicability of the materials for its real-time deployment and better electronic interfacing to develop future electronics with much precision. The linear fitting of two regions were done separately in accordance to Freundlich model, and the Freundlich constants, *k* and *α*, were determined and reported in Table 6 for both adsorption regimes of as prepared $ZnSnO_3$ samples.

As shown in Table 4.6, the value α for all samples is near to unity within low RH range (5%-52%), indicating that all the $ZnSnO_3$ nanostructures have a strong affinity for water vapor. But this value increases from 1.11 to 1.26 by changing the sequence from S-01 to S-02 and suddenly it decreases down to 0.93 for S-03, 0.9 for S-04 and again it increases to 1.42 for S-05 indicates the water affinity. Conversely, in the high RH regimes, the α values obtained are 1.93(S-01),1.88(S-02), 1.95(S-03), 1.95 (S-04) and 1.98(S-05). The highest α value obtained for S-05 was 1.98 shows its adsorption affinity towards vapor. This consistent α value for all samples, indicates a higher adsorption regime at high RH values are comparable with smooth adsorption intensification for the samples at lower RH regime. The calculated k value represents the water adsorption capacity at particular RH state. In the low RH regime, the $ZnSnO_3$ samples showed a randomness in the value starting from 2.06 to 4.86 for S-01 to S-02 followed by 1.16 for S-02 and S-03 and then increase to attain a value of 8.39(S-05). Whereas in the high RH regime, we found k values were much consistent when sample goes from S-01 to S-05 and the highest value obtained is 5.78 for S-05.

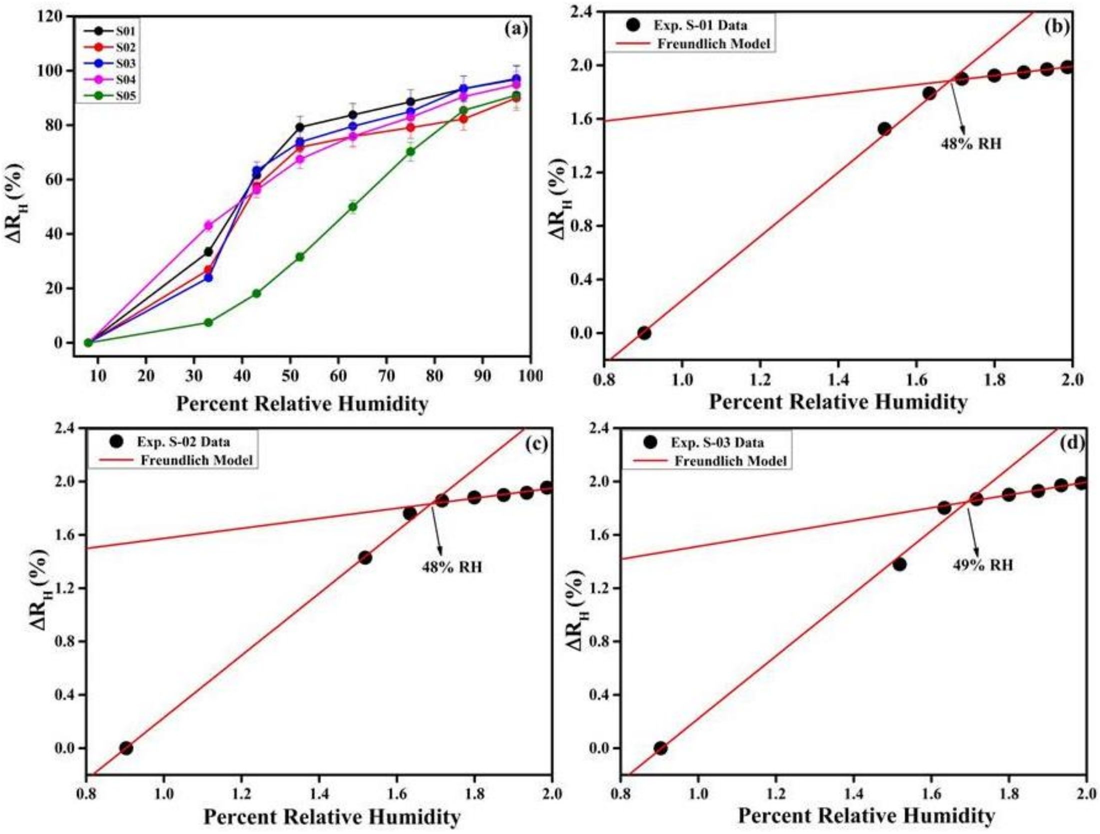

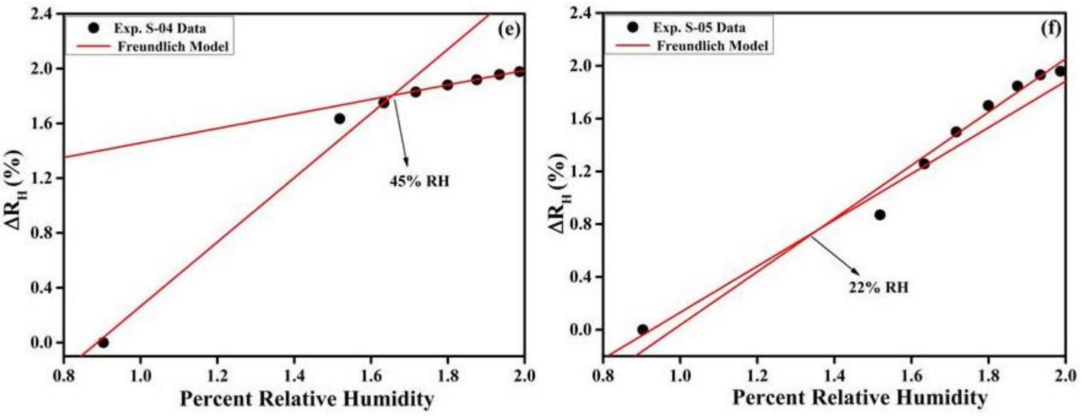

Figure 4.12 Log-Log plot of (a) measured Relative Deviation in resistance (ΔRH) vs. percent relative humidity of 400°C annealed $ZnSnO_3$ samples and individually modelled (Freundlich) behaviour of measured R.D.R vs. percent relative humidity for (b) S-01 (c) S-02, (d) S-03, (e) S-04 and (f) S-05 400°C annealed $ZnSnO_3$ samples.

Using equation 4.3, within the range of investigation, the variation in RDR extended up to 96.8%, 89.9%, 97.1%, 94.8% and 91% respectively for the 400°C annealed $ZnSnO_3$ samples noted through S-01 to S-05 from its initial resistance value respectively. Figure 4.12 (a) shows the combined plot of all the annealed samples measured RDR vs. RH.

Table 4.7 Results from Freundlich Adsorption Model including the Adsorption Capacity (k), Adsorption Strength (α), R^2 value on humidity sensing of 400°C annealed $ZnSnO_3$ samples.

Sample No.	Low RH Regime			High RH Regime		
	k	α	R^2	k	α	R^2
1	1.40 ±0.12	2.39 ±0.08	0.99614	2.04 ±0.01	0.34 ±0.02	0.99771
2	1.57 ±0.14	0.37 ±0.07	0.88095	1.26 ±0.11	2.33 ±0.07	0.99676
3	1.33 ±0.18	2.34 ±0.12	0.99109	1.07 ±0.08	0.48 ±0.04	0.97226
4	1.20 ±0.31	2.34 ±0.21	0.97502	8.45 ±0.05	0.52 ±0.02	0.99144
5	4.19 ±0.34	1.75 ±0.23	0.94996	9.60 ±0.34	2.01 ±0.18	0.95773

The Fig.4.12 (b-f) shows the experimental water adsorption data plotted for individual 400°C annealed sample in the linear format of the Freundlich model with two separate adsorption regions one at lower RH values (5%-52%) and another one at higher RH values (52%-97). The transition point (T_c) was determined by calculating the point where the two linear fits cross each other. The transition point ($\mathrm{T_c}$) for the samples separating both adsorption regimes were found to be 48%, 48%, 49%, 45% and 22% for samples S-01, S-02, S-03, S-04 and S-05 respectively. The lowering of T_c value for 400°C annealed samples than that 250°C annealed samples confirms the increasing potential of the materials.

The linear fitting of two regions were done separately in accordance to Freundlich model, and the Freundlich constants, k and α, were determined and reported in Table 4.7 for both adsorption regimes of as prepared $ZnSnO_3$ samples. As shown in Table 4.7, the value α for all samples is nearly above unity within low RH range (5%-52%), indicating that all the $ZnSnO_3$ nanostructures have a strong affinity for water vapor. The lowest α value obtained is for S-02 which comes around 0.37, whereas for the other annealed samples it goes above unity stating the water affinity in low RH regime. Conversely, in the high RH regimes, the α values follows a random trend with highest α value obtained is 2.33 for S-02 and lowest one is 0.34 for S-01, confirming the high RH region as weaker adsorption region in case of 400°C annealed samples.

The k values calculated from Freundlich isotherm represents the water adsorption capacity at particular RH state. In the low RH regime, the heat treated $ZnSnO_3$ samples showed k values 1.40(S-01), 1.57 (S-02), 1.34(S-03), 1.20(S-04) and highest value of 4.19 for S-05. Whereas in the high RH regime, although k values lie above unity like 2.04(S-01), 1.26(S-02) and 1.07(S-03) goes further up to a value of 8.45(S-04) and 9.6 for S-05 samples confirms the higher adsorption capacity of annealed materials for better performance.

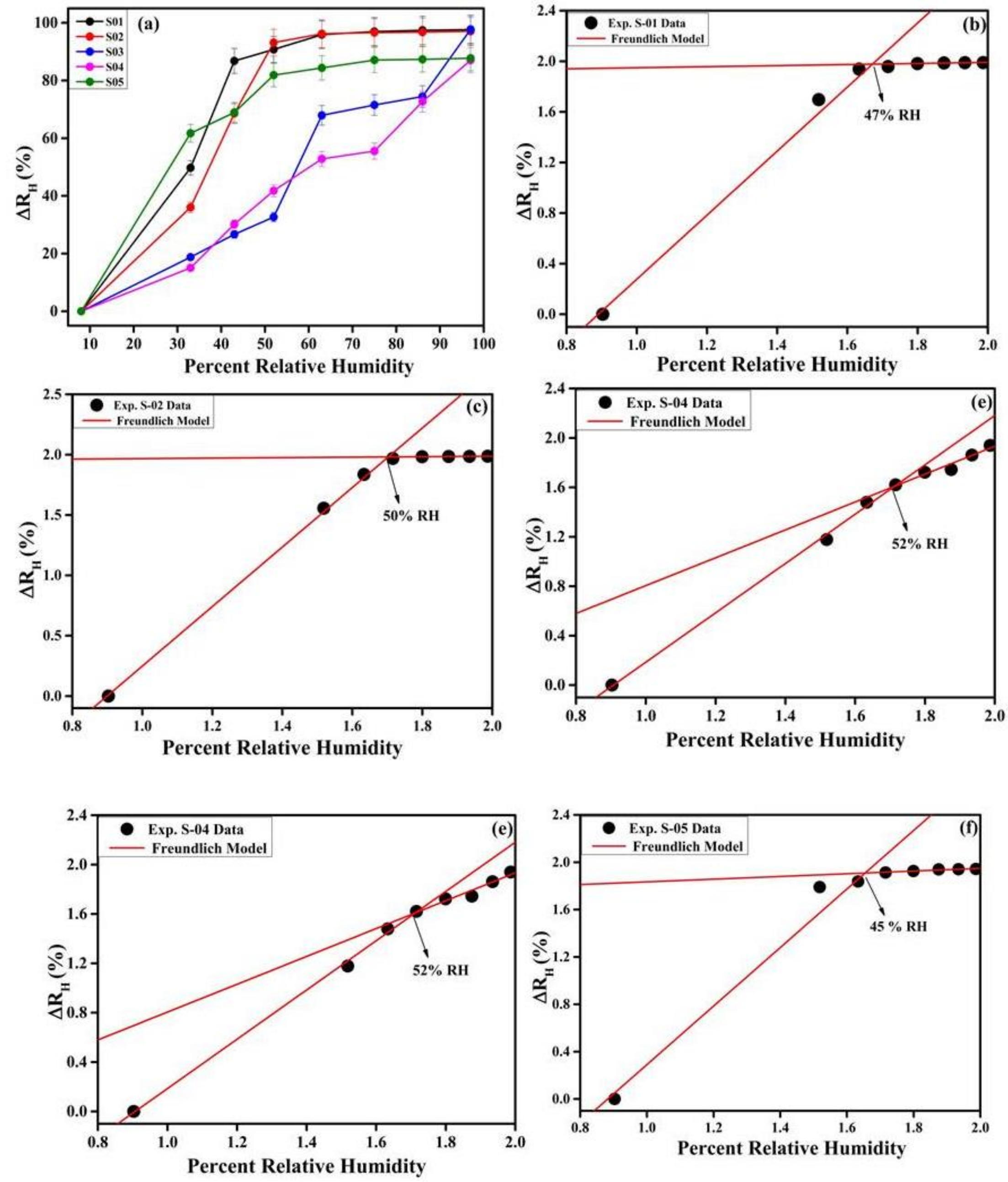

Figure 4.13 Log-Log plot of (a) measured Relative Deviation in resistance (ΔR_H) vs. percent relative humidity of 500°C annealed $ZnSnO_3$ samples and individually modelled (Freundlich) behaviour of measured R.D.R vs. percent relative humidity for (b) S-01 (c) S-02, (d) S-03, (e) S-04 and (f) S-05 500°C annealed $ZnSnO_3$ samples.

Table 4.8 Results from Freundlich Adsorption Model including the Adsorption Capacity (k), Adsorption Strength (α), R^2 value on humidity sensing of 500°C annealed $ZnSnO_3$ samples.

Sample No.	Low RH Regime			High RH Regime		
	k	α	R^2	k	α	R^2
1	8.06 ±0.01	0.94 ±0.07	0.91069	1.79 ±0.29	0.95 ±0.20	0.98121
2	1.64 ±0.09	2.46 ±0.06	0.9978	8.86 ±0.03	0.91 ±0.02	0.97317
3	9.56 ±0.74	1.49 ±0.40	0.76525	5.15 ±0.16	1.91 ±0.11	0.99006
4	2.10 ±0.27	1.12 ±0.14	0.93424	6.45 ±0.08	1.99 ±0.05	0.99742
5	5.25 ±0.03	0.91 ±0.02	0.88526	9.52 ±0.43	2.47 ±0.29	0.95782

Using equation 4.3, the variation in RDR extended up to 97.65%, 97.06%, 97.71%, 87.01% and 87.73% respectively for the 500°C annealed $ZnSnO_3$ samples ascribed as S-01, S-02, S-03, S-04and S-05 from its initial resistance value respectively. Figure 4.13 (a) shows the combined plot of all the annealed samples measured RDR vs. RH. The Fig.4.13 (b-f) shows the experimental water adsorption data plotted for individual 500°C annealed sample in the linear format of the Freundlich model with two separate adsorption regions one at lower RH values (5%-52%) and another one at higher RH values (52%-97). The transition point (T_c) was determined by calculating the point where the two linear fits cross each other. The transition point (T_c) for the samples separating both adsorption regimes were found to be 47%, 50%, 52%, 52% and 45% for samples S-01, S-02, S-03, S-04 and S-05, respectively. The linear fitting of two regions were done separately in accordance to Freundlich model, and the Freundlich constants, k and α, were determined and reported in Table 4.8 for both adsorption regimes of as prepared $ZnSnO_3$ samples. As shown in Table 4.8, the value α for all samples is near to unity within low RH range (5%-52%), indicating that all the $ZnSnO_3$ nanostructures have a strong affinity for water vapor. The lowest α value obtained is for S-05 which comes around 0.91, whereas for the other annealed samples it goes above unity stating the water affinity in low RH regime. Conversely, in the high RH regimes, the α values increases with changing the sample from S-01 to S-05, with highest α value obtained is 2.47 for S-05 and lowest one is 0.91 for S-01, confirming the high RH region as weaker adsorption region in case of 500°C annealed samples. The k values calculated from Freundlich isotherm represents the water adsorption capacity at particular RH state. In the low RH regime, the heat treated $ZnSnO_3$ samples showed *k* values 8.06(S-01), 1.64 (S-02), 9.56 (S-03), 2.1(S-04) and 5.25 for S-05. Whereas in the high RH regime, although *k* values lie above unity like 1.79 (S-01), 8.86 (S-02), 5.15(S-03), 6.45(S-04) and 9.52 for S-05 samples confirms the higher adsorption capacity of annealed materials for better performance.

4.5. Stability of Humidity Sensors

In order to evaluate the reliability, stability tests of the sensor were carried out. Fig. 4.14-4.17 shows the long-term stability of the $ZnSnO_3$ sensors where the resistance *vs.* time characteristics of the sensor were measured within a time interval of 10 days upto 2 months for different concentrations of humidity and the variation is within permissible limit. Figure 4.14 shows the long-term stability test result of as prepared $ZnSnO_3$ samples prepared at different stirring temperature i.e. at S-01(25°C), S-02(45°C), S-03(65°C), S-04(85°C) and S-05(100°C). The results revealed that resistance value at 8% RH value are 42.63kΩ, 35.03 kΩ, 15.21 kΩ, 8.53 kΩ and 5.03 kΩ for S-01, S-02, S-03, S-04 and S-05 respectively. The samples at 97% RH shows resistance of 6.76 kΩ, 3.88 kΩ,3.28 kΩ, 1.25 kΩ and 1.26 kΩ respectively for samples from S-01 through S-05.

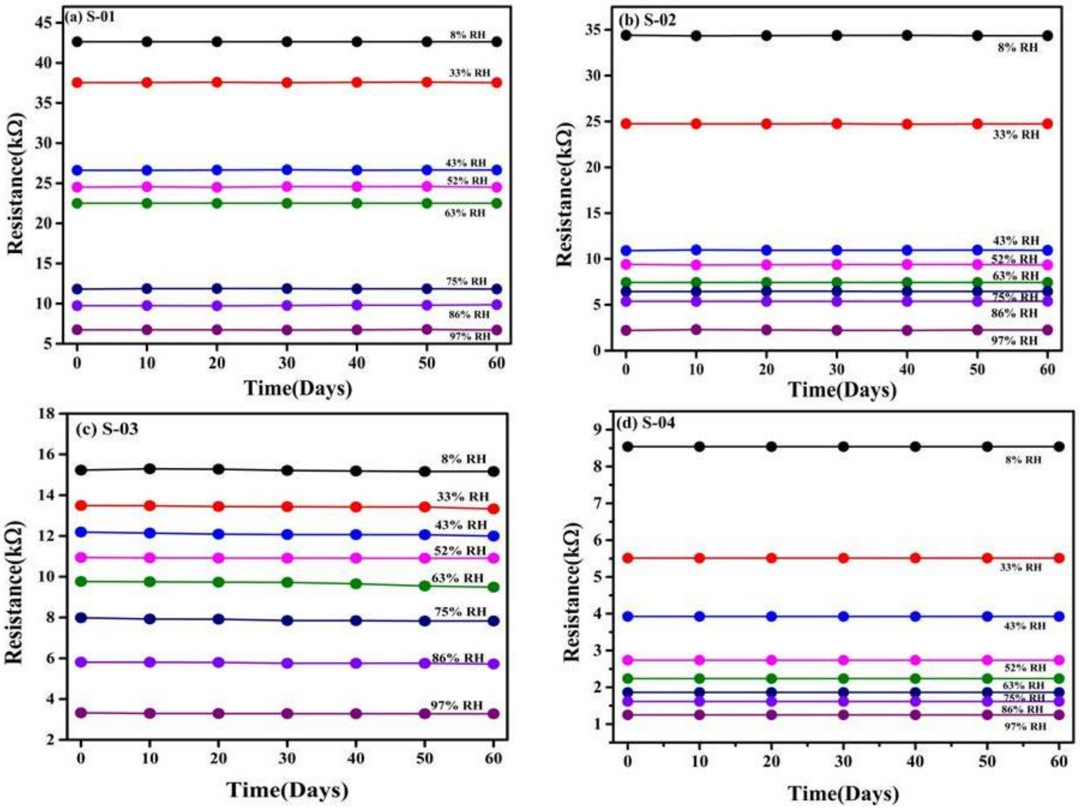

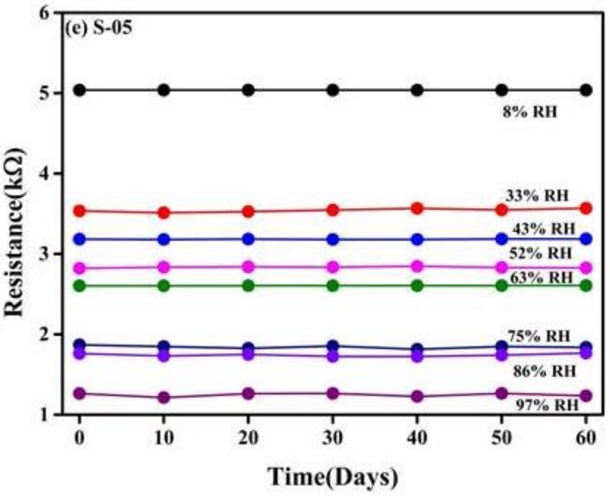

Figure 4.14 Long term stability of as prepared $ZnSnO_3$ samples noted as (a) S-01, (b)S-02, (c) S-03, (d) S-04 and (e) S-05 sensors with the RH% in the range of 08-97% at room temperature.

The resistance value of all samples shows a trend of decrease in the value by going from S-01 to S-05 samples even at lower relative humidity level suggests the effect of stirring temperature over the material and its capacity to adsorb water molecules. Similarly, it is also noted that as going from lower RH (8% RH) to higher RH (97% RH) value the samples shows a maximum decrease in the resistance value due to the water vapor adsorbed the material surface. The Figure 4.14 shows a negligible change in resistance value for individual samples within the test period of 60 days at various humidity level.

Figure 4.15 shows the long-term stability test result of $ZnSnO_3$ samples annealed at 250°C. The samples named with same context followed by that for as prepared samples at different stirring temperature *i.e.* at S-01(25°C), S-02(45°C), S-03(65°C), S-04(85°C) and S-05(100°C). The results revealed that resistance value at 8% RH value are 21.06kΩ, 18.95 kΩ, 12.53 kΩ, 8.19 kΩ and 7.15 kΩ while at 97% RH the values are 4.45 kΩ, 6.53 kΩ,2.6 kΩ, 3.51 kΩ and 1.406 kΩ for S-01, S-02, S-03, S-04 and S-05 respectively. It has been observed that the resistance values in this case is even lower than that of as prepared samples is attributed to the annealing effect.

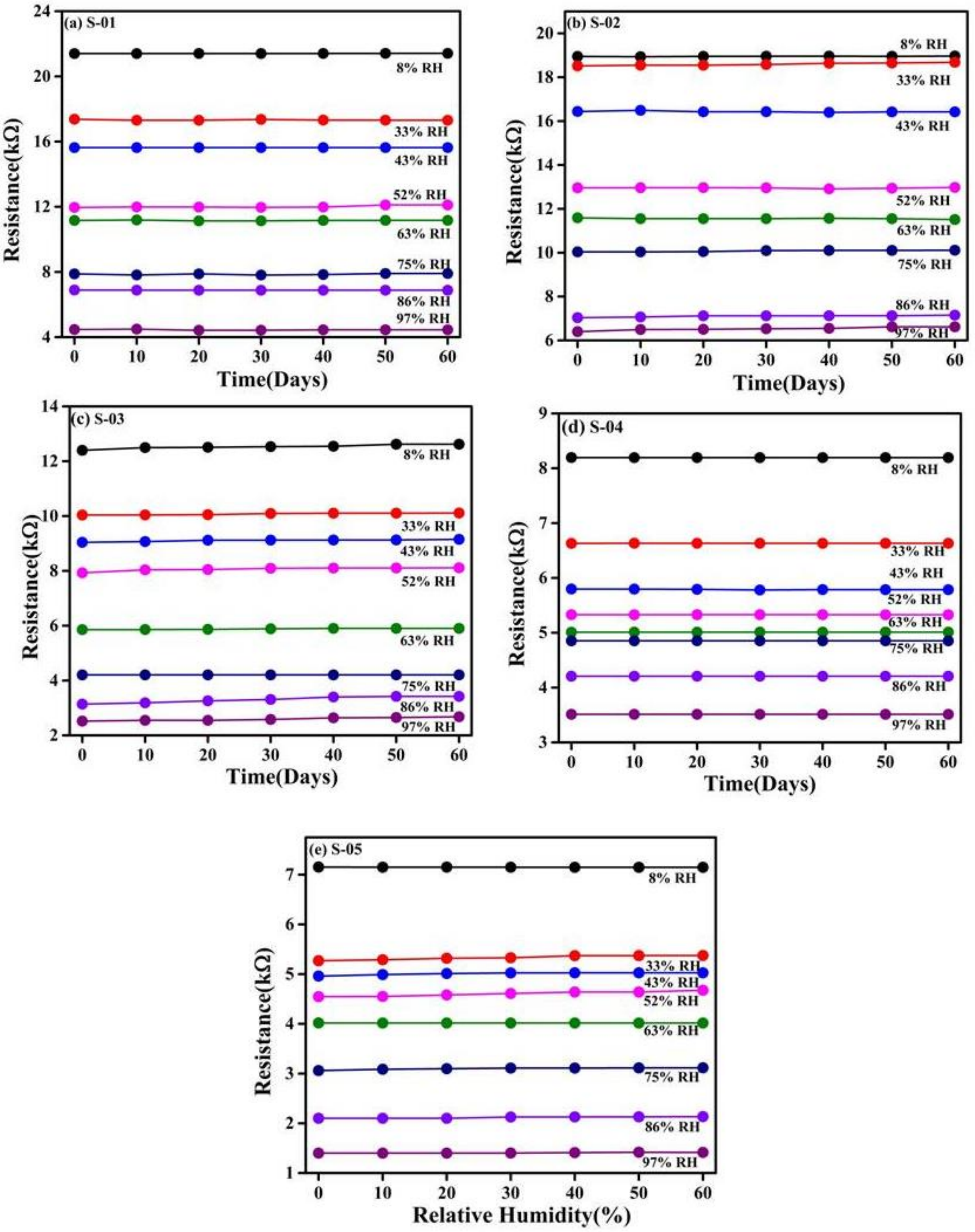

Figure 4.15 Long term stability of 250°C annealed $ZnSnO_3$ samples (a) S-01, (b) S-02, (c)S-03, (d) S-04 and (c)S-05 sensors with the RH% in the range of 08-97%

The decrease in resistance value at high RH is due to the water vapor adsorbs over the material surface. The Figure 4.15 shows a negligible change in resistance value for individual samples within the test period of 60 days at various humidity level. Here it is observed that for S-01 and S-02 the resistance values were coming closer in case of high RH region, while there is no such discrepancy happening in case of S-03, S-04 and S-05 where the resistance values are much well defined and not merging with each other.

Figure 4.16 shows the long-term stability test result of $ZnSnO_3$ samples annealed at 400°C. The samples named with same context followed by that for as prepared samples at different stirring temperature i.e. at S-01(25°C), S-02(45°C), S-03(65°C), S-04(85°C) and S-05(100°C). The results revealed that resistance value at 8% RH value are 42.15kΩ, 39.12 kΩ, 37.49 kΩ, 17.26 kΩ and 10.52 kΩ while at 97% RH the values are 1.33 kΩ, 3.99 kΩ,1.08 kΩ, 0.88 kΩ and 1.05 kΩ for S-01, S-02, S-03, S-04 and S-05 respectively.

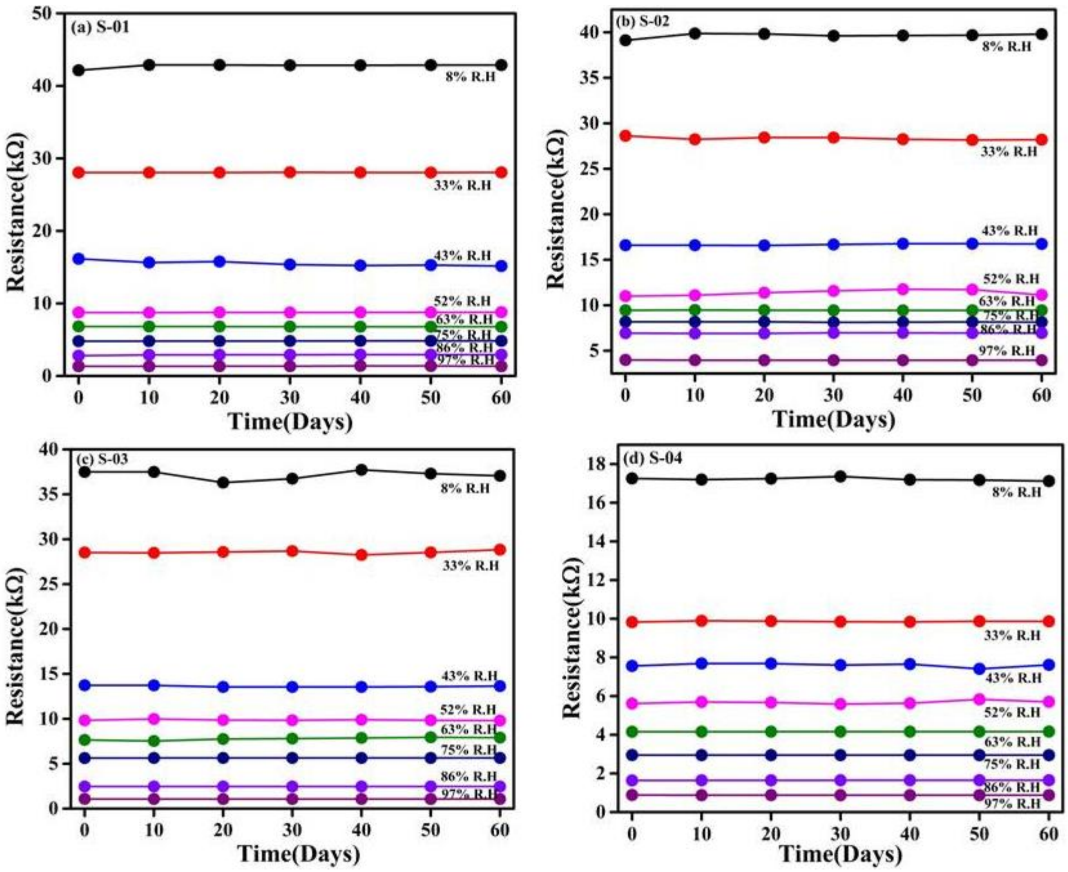

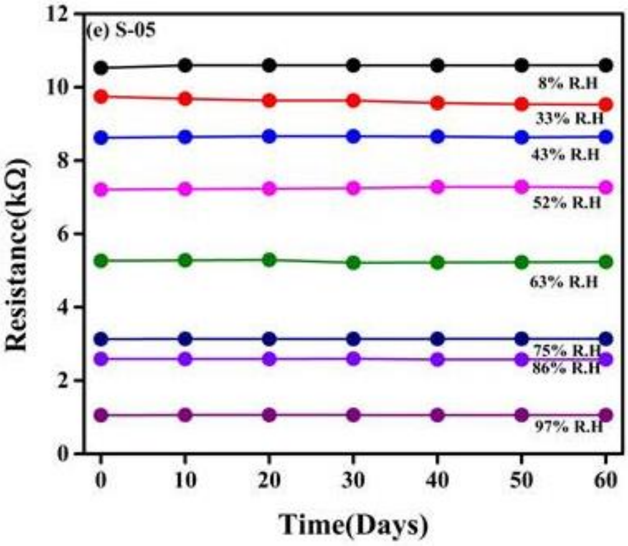

Figure 4.16 Long term stability of 400°C annealed $ZnSnO_3$ samples (a) S-01, (b) S-02, (c)S-03, (d) S-04 and (c) S-05 sensors with the RH% in the range of 08-97%.

The Figure 4.16 shows a marked gap between the resistance values for individual samples within 8-43% RH for the test period of 60 days at various humidity level. Here it is observed that for all the samples the resistance values show appreciable variation in particular relative humidity especially at low RH region which is 8-52% RH. Even the lines connecting the resistance values for samples within test period were in a closest proximity at high RH region which stands for 63-97% RH value. But there is no such discrepancy is observed for S-05 sample where the resistance lines over the period are much distinct in comparison to other candidates of the series.

Figure 4.17 shows the long-term stability test result of $ZnSnO_3$ samples annealed at 500°C. The samples named in same fashion followed by that for as prepared samples synthesized at different stirring temperature i.e. at S-01(25°C), S-02(45°C), S-03(65°C), S-04(85°C) and S-05(100°C). The results revealed that resistance value at 8% RH value are 233.64kΩ, 64.36 kΩ, 29.45 kΩ, 21.55 kΩ and 14.32 kΩ while at 97% RH the values are 5.49 kΩ, 1.88 kΩ,0.6 kΩ, 2.79 kΩ and 1.75 kΩ for S-01, S-02, S-03, S-04 and S-05 respectively.

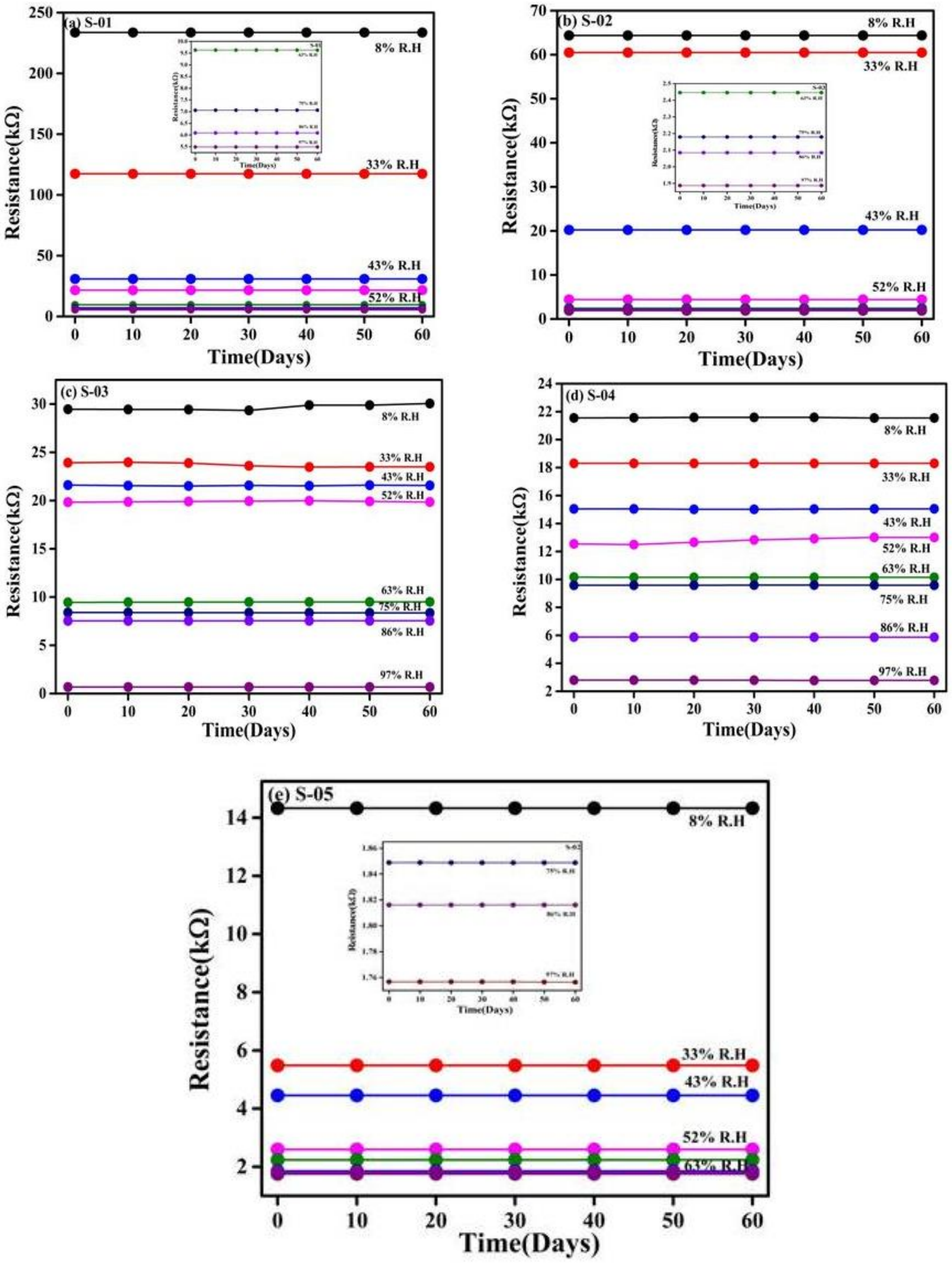

Figure 4.17 Long term stability of 500°C annealed $ZnSnO_3$ samples (a) S-01, (b) S-02, (c)S-03, (d) S-04 and (c)S-05 sensors with the RH% in the range of 08-97%.

From Figure 4.17, it has been observed that the difference between resistance values for samples in this series of 500°C annealed $ZnSnO_3$ is highest than that of other samples in case of as prepared and 250°C and 400°C annealed samples is attributed to the annealing effect which helps the materials surface to adsorb more water vapor and to cause the decrease in resistance at high RH end. The Figure 4.17 shows a negligible change in resistance value for individual samples within the test period of 60 days at various humidity level. In Figure 4.17(a), (b) and (e) the inset shows resistance vs. time plot for S-01, S-02 and S-05 at 63-97% RH value due to the much closeness between the stability lines at high end of relative humidity. Again, it is observed that for all the samples are well classified over the wider time period suggesting its much practical utilization.

4.6. Response-Recovery Study:

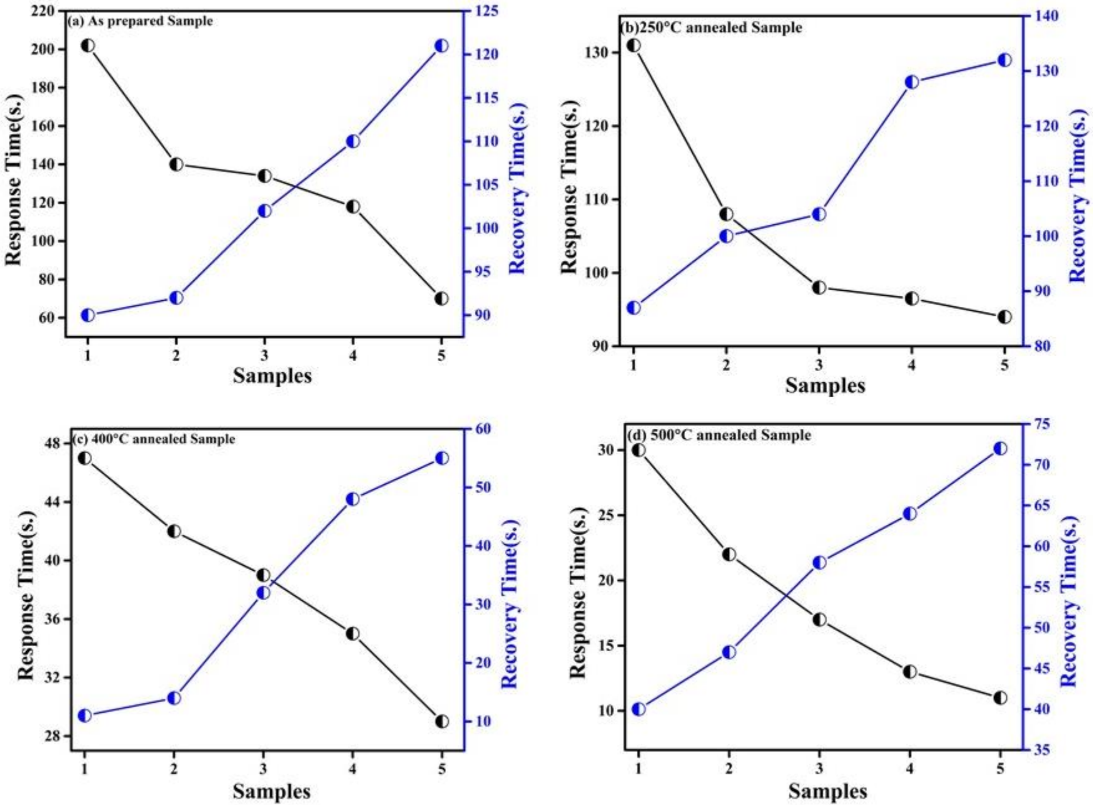

Figure 4.18 Response -Recovery plot of (a) As prepared samples, (b) 250°C annealed samples, (c) 400°C annealed samples and (d) 500°C annealed samples for 08%-97%-08% relative humidity change cycle.

The Figure 4.18 shows the response and recovery time for all the samples bundled under the category of as prepared, 250°C, 400°C and 500°C annealed samples. The response and recovery time of all samples were measured for the cycle of relative humidity change from 8% RH to 97% RH and then returning back to 8% RH. The response and recovery values of the sensor to achieve 90% of the total resistance change was defined by H_2O molecular adsorption and desorption time. Hence the response is defined by the time period required for 90% change in resistance value and the recovery time period was defined by the time period for attaining the same resistance value before the change takes place. Form Fig. 4.18(a) we came to know about the response time of the as prepared $ZnSnO_3$ sensing materials which turned up to be 202,140,134,118 and 70 seconds for S-01 followed through S-05 respectively. Whereas the recovery time nearly follows the opposite behaviour that of response trend which was 90, 92, 102, 110 and 121 seconds, respectively for S-01, S-02, S-03, S-04 and S-05. The decrease in response time and increase in recovery time can be attributed to the stirring temperature at which the materials were synthesized which directly affects the surface property to adsorb and desorb water vapours from the surface during the humidity sensing process. In a similar trend now we looked into 250°C annealed $ZnSnO_3$ samples and study their response-recovery behaviour towards 08%-97%-08% relative humidity change cycle. It was observed that the response time for all the annealed samples were 131,108,98,96.5 and 94 seconds while the recovery time are 87,100,104,128 and 132 seconds respectively for S-01, S-02, S-03, S-04 and S-05. The response and recovery time periods for the annealed samples got improved from that of as prepared samples extends the fact of annealing over the materials and improved surface property required for improvement in sensing.

Figure 4.18(c) culminates the response- recovery behaviour of all the 400°C annealed $ZnSnO_3$ samples. It has been inferred from the Fig.4.18(c) that the response and recovery time are 47s./11s.,42s./14s.,39s./32s.,35s./48s. and 29s./55s. for S-01, S-02, S-03, S-04 and S-05 respectively. The higher annealing temperature implied over the as prepared samples decreased the response/recovery time and helps to improve the sensitivity. Similarly, in the continuation of effect of annealing temperature of 500°C on the $ZnSnO_3$ samples showed that the response/recovery time of 30s /40s, 22s/47s, 17s /58s, 13s./64s. and 11s./72s. respectively, for samples from S-01 to S-05 in turn. The results in Figure 4.18(d) shows that the 500°C annealed the lowest response time period in comparison to the other set of $ZnSnO_3$ samples indicate it as best humidity sensing materials for the experimented relative humidity range.

4.7. Plausible Humidity Sensing Mechanism:

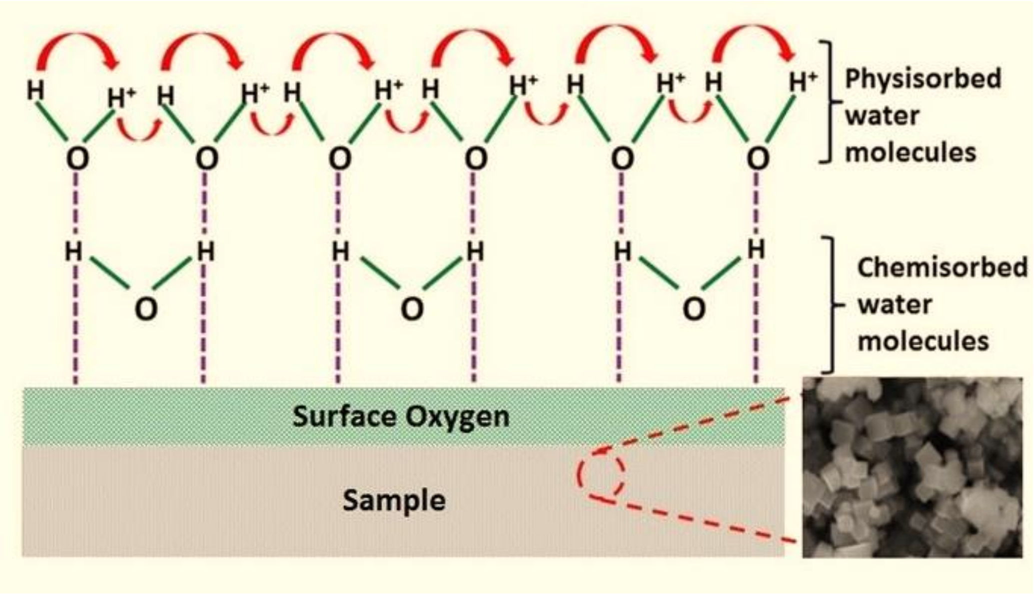

Figure 4.19 Schematic mechanism of humidity sensing observed in Metal Stannates ($ZnSnO_3$)

Kulwicki *et al.*, proposed water related conduction mechanism as a surface mechanism in ceramic and porous materials which includes nearly all metal oxides and most adaptable reason for humidity sensing [25]. Here we provided some discussions about the humidity sensing mechanism of metal stannates i.e. $ZnSnO_3$ in accordance to the available literature, where water molecules act as electron donor contributing towards the conduction mechanism in the oxide semiconductor materials [26]. The humidity sensing at room temperature generally proceeds through two processes (i) chemisorption process for low humidity followed by (ii) Physisorption process at higher humidity level accompanying Grotthuss chain reaction. Generally, at room temperature molecular oxygen adsorbs on the sensor and captures electrons

$(O_2 + e^- \rightarrow O_2^-)$[27].

Schaub *et al.*, proposed that the defects present in the nanorods present a strong enough electrostatic field and localized charge density generated from the pre-adsorbed oxygen ions promotes dissociation of water molecules chemisorbed on the surface resulting into proton as charge carriers for the hopping transport [28]. At higher humidity level, a series of water layers get adsorbed over the surface by physisorption mechanism, the water molecules undergo dissociation to produce hydronium ion $(2H_2O \rightarrow H_3O^+ + OH^-)$. As hydronium ion hydration is energetically favoured in physisorption $(H_2O + H_3O^+ \rightarrow H_3O^+ + H_2O)$, hence act as major charge carrier.

Again, according to Grotthuss mechanism H^+ ions are capable for moving freely in physisorbed water contributes towards the protonic conduction along with the electrolytic conduction due to H_3O^+ towards the variation of resistance in $ZnSnO_3$ nanomaterials during the transfer from low to high humidity range.

It has been reported that doping induced defects on the nanomaterial surface act as adsorption site which helps to transfer the charges between water molecules and nanomaterials enhancing the humidity sensing over the pristine [29]. The fact along with obtained results indicate that humidity-sensing performance improved with annealing, particularly at 400°C and 500°C for humidity range spanning from 08% to 97%. With higher annealing temperature, more free electrons can be generated improving the humidity sensing, as expressed in the following reaction,

$$\mathrm{H_2O} + \mathrm{O_o} + \mathrm{ZnSnO_3} \rightarrow 2(\mathrm{OH} - \mathrm{Zn}) + \mathrm{VO}^{\cdot\cdot} + 2e^{-} \qquad (4.4)$$

Where, O_o is the oxygen ion in the inherent lattice; and $VO^{\cdot\cdot}$ represents the neutrality. Our results show that the increase in annealing temperature possibly creates more defects for possible adsorption sites and promotes easier charge transfer by reducing the hydroxyl ion formation and its interaction with H_3O^+. Hence 500°C annealed samples show more efficient sensing performance than other samples if we compare the response and recovery time to detect the change in ambient humidity over a closed atmosphere bargaining for its much practical usage. These possible reasons for the adsorption and desorption of water molecules are in much closer proximity to that of isotherm model results which earlier stated the variation in conduction behaviour of $ZnSnO_3$ samples and its detailed surface phenomena.

Chapter-5

5. Conclusion and Scope of Work

The successful synthesis of $ZnSnO_3$ nanocrystallites via wet chemical synthesis technique is presented in the report. A wide temperature range of 25-100°C is implemented towards optimizing synthesis parameters which is also in relation with the obtained XRD results showing crystalline phase for all the $ZnSnO_3$ samples. To investigate the effect of annealing on samples prepared only by varying the stirring temperature, annealing temperature of 250°C, 400°C and 500°C is implemented and the primary material characterizations like XRD and FE-SEM shows presence of more uniform and distributed nanocubes.

The thermal analysis of tertiary metal oxides like $ZnSnO_3$ provides much informative decision for the chosen annealing temperature in accordance to the available literature. Similarly, N_2 adsorption-desorption behaviour of synthesized $ZnSnO_3$ samples provides information regarding the pore size distribution of samples lying in the range of 5-50nm *i.e.* mesoporous materials along with surface area distribution from 15-20 m^2/g which are desirable for better sensing results.

The humidity sensing experiments showed that 500°C annealed samples show sensitivity within 700-4500% which is much higher than that of any other annealed samples in the 8-97% RH range. Again, the other device aspects of materials like hysteresis and relative deviation in resistance has been carried out for all the samples. It suggested that the 500°C annealed samples shows least hysteresis value of nearly in 0.00000305 to 0.001 within subjected RH values confirms its practical usage with nearly no significant interference which is highly desired for any material for its implementation in device. Relative Deviation in Resistance (R.D.R) which infers about the electronic interfacing of any humidity sensing materials showed that the annealed samples show much specific trend of increase in the value with increase in RH value from 08% to 97%. Freundlich isotherm modelling of the R.D.R values against applied relative humidity values for the samples provides resemblance of two different adsorption regimes present in humidity sensing according to plausible humidity sensing mechanism.

Again, the modelling of samples towards Freundlich adsorption isotherm resulted into the deeper insight of adsorption capacity and adsorption strength of $ZnSnO_3$ samples towards water vapours. The 500°C annealed samples shows adsorption capacity values of 1.5-9.5 and 1.7-8.9 in low RH (8%-53%) and high RH (53-97%) region along with adsorption strength of 0.9-2.5 for both the RH regions provides plausible water adsorption and desorption mechanism in sensing process.

Stability of all $ZnSnO_3$ samples were checked for more than 8-9 weeks and confirmed that our humidity sensing materials provide nearly no deviation from the initial value from starting day of experiment in same RH value. The response time and recovery time of all the samples were noted down for the cycle of 08%-97%-08 % RH to check the sensing ability of materials. It has been observed that the response time decreases from 202 secs. to 11 secs. by moving from as prepared to 500°C annealed samples. Along with improved recovery time period from 120 secs. to 40 secs. The collective results suggest that annealed samples of $ZnSnO_3$ have the potential to constitute as next generation humidity sensors with much better precision.

REFRENCES

1. (i) Song, X., Qi, Q., Zhang, T., Wang, C. (2009) A humidity sensor based on KCl-Doped SnO_2 nanofibers, Sens. Actuators, B 138, 368–373. (ii) Traversa, E. (1995), Ceramic sensors for humidity detection: the state-of-the-art and future developments, Sens. Actuators, B 23, 135-156.
2. Yao, W., Chen, X., Zhang, J. (2010) A capacitive humidity sensor based on gold–PVA core–shell nanocomposites. Sens. Actuators, B, 145, 327–333.
3. (i) Zampetti, E., Pantalei, S., Pecora, A., Valletta, A., Maiolo, L., Minotti, A., Macagnano, A., Fortunato, G., Bearzotti, A., (2009) A Design and optimization of an ultra-thin flexible capacitive humidity sensor. Sens. Actuators, B, 143, 302–307. (ii) Mai, L.H., Hoa, P.M., Binh, N.T., Ha, N., An, D.K., (2000) Some investigation results of the instability of humidity sensors based on alumina and porous silicon materials, Sens. Actuators, B 66, 63-65.
4. Wei, J., Yue, C., Van Der Velden, M., Liu Z.W., Makinwa, K.A.A., Sarro, P.M. (2010) Design, fabrication and characterization of a femto-farad capacitive sensor for picoliter liquid monitoring. Sens. Actuators, A, 162, 406–417.
5. Carminati, M., Ferrari, G., Guagliardo, F., Sampietro, M., (2010) ZeptoFarad capacitance detection with a miniaturized CMOS current front-end for nanoscale sensor. Sens. Actuators, A, 172, 117–123.
6. Aezinia, F., Wang, Y., Bahreyni, B. (2012) Three-dimensional touchless tracking of objects using integrated capacitive sensors. IEEE Trans. Consum. Electron., 58, 886–890.
7. Chen, Z., Lu, C. (2005) Humidity Sensors: A Review of Materials and Mechanisms, Sens. Lett., 3, 274–295.
8. Ansbacher, F. and Jason, A. C., (1953) Effects of Water vapour on the Electrical Properties of Anodized Aluminium, Nature, 24, 177-178.
9. Thorp, J. M., (1959) The Dielectric Behaviour of Vapours Adsorbed on Porous Solids, Trans. Faraday Soc. 55, 442-454.
10. Gong, M. S., Park, J. S., Lee, M. H., Rhee, H. W., (2002) Humidity sensor using cross-linked polyelectrolyte prepared from mutually reactive copolymers containing phosphonium salt, Sens. Actuators, B 86, 160-167.

11. Varghese, O. K., Grimes, C. A., (2003) Metal oxide nanoarchitectures for environmental sensing, J Nanosci Nanotechnol.,3, 277-293.
12. Shamala, K. S., Murthy, L. C. S., Rao, K. N., (2004) Studies on optical and dielectric properties of Al_2O_3 thin films prepared by electron beam evaporation and spray pyrolysis method, Mater. Sci. Eng. B, 106, 269-274.
13. Greenspan, L., (1977) Humidity fixed points of Binary Saturated Aqueous Solutions, *J. Res. Nat. Bur. Stand.,* 81A,89–96.
14. Lide, D. R., (2009) *CRC Handbook of Chemistry and Physics,* 91st edn., CRC Press, Boca Raton, Florida, USA.
15. Zhang, D., Chang, H., Liu, R., (2016) Humidity sensing properties of one-step hydrothermally synthesized Tin dioxide-decorated graphene nanocomposite on polyimide substrate, Journal of Elec Materi, 45, 4275-4281.
16. Chen, L.T., Lee. C.Y., Cheng, W.H., (2008) MEMS-based humidity sensor with integrated temperature compensation mechanism, Sens. Actuators, A, 147, 522-528.
17. Pawbake, A.S., Waykar, R., Late, D.J., Jadkar, S.R., (2016) Highly transparent wafer scale synthesis of crystalline WS_2 nanoparticle thin film for photodetector and humidity sensing applications, ACS Appl. Mater. Interfaces, 5, 3359–3365.
18. Kannan, P.K., Late, D.J., Morgan, H., Rout, C.S., (2015) Recent Developments in 2D Layered Inorganic Nanomaterials for Sensing, Nanoscale, 7, 13293– 13312.
19. Herran, J., Fernandez, I., Ochoteco, E., Cabanero, G., Grande, H., (2014) The role of water vapour in ZnO nanostructures for humidity sensing at room temperature, Sens. Actuators, B ,198, 239-242.
20. Tomer, V.K., Thangaraj, N., Gahlot, S., Kailasam, K., (2016) Cubic mesoporous Ag@CN: a high-performance humidity sensor, Nanoscale, 8, 19794-19803.
21. Tsai, F.S., Wang, S.J., (2014) Enhanced-sensing performance of relative humidity sensors using laterally grown ZnO nanosheets, Sens. Actuators, B, 193, 280-287.
22. Yadav, B.C., Srivastava, R., Dwivedi, C.D., Pramanik, P., (2009) Synthesis of nano-sized ZnO using drop wise method and its performance as moisture sensor, Sens. Actuators, A,153, 137-141.

23. Peng, X., Chu, J., Yang. B., Feng, P.X., (2012) Mn-doped zinc oxide nanopowders for humidity sensors, Sens. Actuators, B, 174, 258–262.
24. Sharma, A., Bhojane, P., Rana, A.K., Kumar, Y., Shirage, P.M., (2017) Mesoporous nickel cobalt hydroxide/oxide as an excellent room temperature ammonia sensor, Scripta Materialia ,128, 65-68.
25. Xu, C.H., Shi, S.Q., Surya, C., (2008) Gas sensors based on one-dimensional nanostructures, Sensors, 9, 9903-9924.
26. Hatch, C.D., Wiese, J.S., Crane, C.C., Harris, K. J., Kloss, H.G., Baltrusaitis, J., (2012) Water Adsorption on Clay Minerals as a Function of Relative Humidity: Application of BET and Freundlich Adsorption Models, Langmuir, 28, 1790-1803.
27. Kulwicki, B.M., (1991) Humidity sensors, J. Am. Ceram. Soc. 74 ,697–708.
28. Morrison, S.R., (1982) Semiconductor gas sensors, Sens. Actuators, 2 ,329-341.
29. Schaub, R., Thostrup, P., Lopez, N., Lagsgaard, E., Stensgaard, I., Norskov, J.K., Besenbacher, F., (2001) Oxygen vacancies as active sites for water dissociation on rutile TiO_2 (1 1 0), Phys. Rev. Lett., 87, (266104/1–266104/4). (ii) Chow, L.L., Yuen, M.M.F., Chan, P.C.H., Cheung, A.T., (2001) Reactive sputtered TiO2 thin film humidity sensor with negative structure bias, Sens. Actuators B, 76, 310-315.
30. Aziz, S., Bum, K.G., Yang, Y.J., Yang, B.S., Kang, C.U., Doh, Y.H., Choi, K.H., Kim, H.C., (2016) Fabrication of $ZnSnO_3$ based humidity sensor onto arbitrary substrates by micro-Nano scale transfer printing, Sens. Actuators, A, 246, 1-8.
31. Li, J., Fu, T., Chen, Y., Guan, B., Zhuo, M., Yang, T., Xu, Z., Li, Q., Zhang, M., (2014) Highly sensitive humidity sensors based on Sb-doped $ZnSnO_3$ nanoparticles with very small sizes, CrystEngComm, 16, 2977-2983.
32. Md Sin, N.D., Khadijah, N., Mamat, M.H., Musa, M.Z., Rusop, M., (2012) Influence of Cubic Structured-$ZnSnO_3$ Immersion Time to the Performance of Humidity Sensor, Nano Hybrids, 2, 1-11.
33. Yadav, B. C., Singh, R., Singh, S., Dwivedi, P. K., (2012) Humidity Sensing Investigations on Nanostructured Zinc Stannate Synthesized via Chemical Precipitation Method, International Journal of Green Nanotechnology, 4, 37-45.

34. Bauskar, D., Kale, B. B., Patil, P., (2012) Synthesis and humidity sensing properties of $ZnSnO_3$ cubic crystallites, Sens. Actuators B, 161, 396-400.